Computers and Structures 329 (2026) 108290

Contents lists available at ScienceDirect

Computers and Structures

journal homepage: www.elsevier.com/locate/compstruc

A computational approach to electromechanical coupling by eddy currents in vibrating beams

Mikel Brun *, Fernando Cortés, María Jesús Elejabarrieta

Department of Mechanics, Design and Industrial Management, University of Deusto, Avda. de las Universidades 24, 48007 Bilbao, Spain

ARTICLE INFO

Keywords:
Eddy current damping
Electromagnetic-mechanical coupling
Bending-torsion coupling
Multiphysics dynamics

ABSTRACT

The dynamic behaviour of conductive beams subjected to magnetic fields involves complex interactions between mechanical motion and induced electromagnetic forces. This study introduces a coupled computational approach that captures the mechanisms of eddy current damping and their role in vibration attenuation and bending-torsion coupling of thin, non-magnetic conductive beams. The structural response is modelled using finite elements that include bending and torsional degrees of freedom, while the electromagnetic effects generated by motional induction are evaluated through a finite difference formulation. The resulting velocity-dependent electromagnetic forces are integrated directly into the dynamic equations of motion, resulting in a symmetric but non-proportional damping matrix governing both energy dissipation and cross-coupling between vibration modes. The proposed formulation is further validated against experimental data, confirming its ability to accurately reproduce the observed dynamic response. Frequency- and time-domain simulations reveal that increasing magnetic field magnitude enhances vibration attenuation, and that bending-torsion coupling arises only when magnetic fields are oriented in multiple directions. The proposed model provides a systematic means to investigate electromagnetic–mechanical coupling mechanisms in beam-like structures and to predict their dynamic performance under magnetic fields, offering new insights and computational tools for non-contact vibration control in advanced mechanical systems.

1. Introduction

The attenuation of mechanical vibrations in structural systems is of paramount importance, as their presence can lead to structural failures, discomfort, reduced performance, and decreased lifespan of structural components [1]. Vibration mitigation can be achieved through the implementation of various damping techniques. Among them, eddy current damping, originating from Foucault currents, provides an effective and contactless vibration control mechanism. These currents can be generated when mechanical vibrations interact with an externally applied magnetic field, a phenomenon referred to as motional induction. The induced currents, in turn, produce electromagnetic forces that, when suitably aligned with the motion, include components opposing it, thereby reducing vibration amplitudes [2].

Eddy current damping offers several advantages: high efficiency at low frequencies, reversibility, absence of wear, instantaneous application, and no added mass due to its non-contact nature [3]. For these reasons, extensive research has explored diverse engineering applications where this damping mechanism can be beneficial [4–7].

Despite its advantages, two fundamental challenges arise in the mathematical analysis of eddy current damping within vibrating mechanical systems. Firstly, the electromagnetic phenomenon (eddy currents) and the mechanical response (structural vibrations) are inherently coupled. Consequently, the electromagnetic or Lorentz forces must be incorporated into the dynamic equations of motion, which is non-trivial due to the spatial and temporal complexity of eddy currents. Secondly, the resulting coupled equations are generally not analytically solvable, making numerical methods essential to determine the induced currents and their associated damping effects.

To address these challenges, significant research efforts have been devoted to addressing the numerical challenges associated with eddy current damping. In 1986, the international working group “Testing Electromagnetic Analysis Methods” (TEAM) established a set of benchmark problems to evaluate the accuracy and reliability of numerical methods in solving complex electromagnetic problems. Among these, TEAM Problem 12, which was focused on motional induction, has contributed to the development of various numerical formulations. For instance, comparisons between different formulations based on finite element, boundary integral, and finite difference methods for solving

* Corresponding author.
E-mail addresses: mikel.brun@opendeusto.es (M. Brun), fernando.cortes@deusto.es (F. Cortés), maria.elejabarrieta@deusto.es (M.J. Elejabarrieta).

https://doi.org/10.1016/j.compstruc.2026.108290
Received 10 February 2026; Accepted 16 May 2026
Available online 28 May 2026

Nomenclature

Variables

b beam width
B_x, B_y external, uniform, magnetic field components in the x- and y-directions, respectively
$B_x(x,y), B_y(x,y)$ external, non-uniform, magnetic field components in the x- and y-directions, respectively
$B_x^{l,k}, B_y^{l,k}$ magnetic field components in the x- and y-directions, respectively, at the (l,k) - th cell
$B_{x,1}^{n,m}, B_{x,2}^{n,m}, B_{x,3}^{n,m}, B_{x,4}^{n,m}, B_{y,1}^{n,m}, B_{y,2}^{n,m}, B_{y,3}^{n,m}, B_{y,4}^{n,m}$ magnetic field components in the x- and y-directions, respectively, at the cells surrounding the (n,m) - th cell corner
$\boldsymbol{B}_\mathrm{e}(x,y)$ external, time-invariant magnetic flux density vector field
$\boldsymbol{B}_\mathrm{i}(x,y,t)$ magnetic flux density vector field induced by the eddy currents through self-inductance
$\boldsymbol{C}$ electromagnetic–mechanical coupling damping matrix
d beam thickness
$\mathrm{d}\boldsymbol{l}$ differential length vector along C
$\mathrm{d}\boldsymbol{l}_1^{n,m}, \mathrm{d}\boldsymbol{l}_2^{n,m}, \mathrm{d}\boldsymbol{l}_3^{n,m}, \mathrm{d}\boldsymbol{l}_4^{n,m}$ differential length vectors of each side of the contour C associated to the (n,m) - th cell corner
$\mathrm{d}\boldsymbol{S}$ elementary surface area vector of S
$\boldsymbol{D}_1, \boldsymbol{D}_2, \boldsymbol{D}_3, \boldsymbol{D}_4, \boldsymbol{D}_5, \boldsymbol{D}_6, \boldsymbol{D}_7$ intermediate electromagnetic forces matrices
E Young's modulus of the beam material
f frequency
$\boldsymbol{f}_\mathrm{em}(x,y,t)$ electromagnetic force density vector field
$\boldsymbol{F}_\mathrm{em}(t)$ nodal electromagnetic force vector
$F_{\mathrm{em,cell}}^{l,k}(t)$ electromagnetic force at the (l,k) - th cell
$F_{\mathrm{em,cell},1}^{l,k}(t), F_{\mathrm{em,cell},2}^{l,k}(t)$ electromagnetic forces at the left and right cell edges, respectively, of the (l,k) - th cell
$\boldsymbol{F}_\mathrm{em,cells}(t)$ vector containing the electromagnetic forces at the cell centres
$F_{\mathrm{em},j}(t)$ electromagnetic nodal force at the j-th node
$\boldsymbol{F}_\mathrm{ext}(t)$ nodal external forces vector
$\boldsymbol{F}_\mathrm{ext}(x,y,t)$ external forces vector field
G shear modulus of the beam material
h_x finite element and finite difference cell size in the x-direction
h_y finite difference cell size in the y-direction
$\boldsymbol{J}(t)$ vector containing the eddy current density at the cell centres
$\boldsymbol{J}(x,y,t)$ eddy current density vector field
$J_x(x,y,t), J_y(x,y,t)$ eddy current density vector fields components in the x- and y-directions, respectively
$J_x^{l,k}(t), J_y^{l,k}(t)$ eddy current components in the x- and y-directions at the (l,k) - th cell
$\boldsymbol{J}^{l,k}(t)$ eddy current density vector at the (l,k) - th cell
$\boldsymbol{K}$ stiffness matrix
L beam length
L_c conductive beam inductance
$\boldsymbol{M}$ mass matrix
$M_{\mathrm{em},x,1}^{l,k}(t), M_{\mathrm{em},x,2}^{l,k}(t)$ electromagnetic moments in the x-direction at the left and right cell edges, respectively, at the (l,k) - th cell
$M_{\mathrm{em},x,j}(t)$ electromagnetic moment in the y-direction at the j-th finite element node
$M_{\mathrm{em},y,1}^{l,k}(t), M_{\mathrm{em},y,2}^{l,k}(t)$ electromagnetic moments in the y-direction at the left and right cell edges, respectively, at the (l,k) - th cell
$M_{\mathrm{em},y,j}(t)$ electromagnetic moment in the y-direction at the j-th finite element node
N total number of finite difference cells
N_x total number of beam finite elements and number of finite difference cells in the x-direction
N_y total number of finite difference cells in the y-direction
$\boldsymbol{q}_j(t), \dot{\boldsymbol{q}}_j(t), \ddot{\boldsymbol{q}}_j(t)$ nodal displacement, velocity and acceleration vectors at the j-th finite element node, respectively
R_c conductive beam resistance
t time
$\boldsymbol{T}(t)$ global vector containing the electric potential at the cell corners
$T(x,y,t)$ scalar field component of $\boldsymbol{T}(x,y,t)$
$\boldsymbol{T}(x,y,t)$ electric potential vector field
$T_1^{l,k}(t), T_2^{l,k}(t), T_3^{l,k}(t), T_4^{l,k}(t)$ electric potentials at the corners of the (l,k) - th cell
$T_1^{n,m}(t), T_2^{n,m}(t), T_3^{n,m}(t), T_4^{n,m}(t)$ electric potentials associated with the (n,m) - th cell corner
$\boldsymbol{T}_\mathrm{edge}(t)$ vector containing the electric vector potentials at the beam surface edges
$\boldsymbol{T}_\mathrm{uk}(t)$ vector containing the unknown electric vector potentials
$T^{n,m}(t)$ electric potential at the (n,m) - th cell corner
$\boldsymbol{T}^{l,k}(t)$ vector containing the electric vector potential at the corners of the (l,k) - th cell
$w(t)$ nodal transverse displacement
$w(x,y,t)$ transverse displacement vector field component
$\boldsymbol{w}(x,y,t)$ transverse displacement vector field
$w_\mathrm{b}(x,t)$ transverse displacement field due to bending
$w_j(t)$ nodal transverse displacement for the j-th node
$w_k(t), w_{k+1}(t)$ transverse displacements at the k-th and $(k+1)$ - th finite element nodes, respectively
$\dot{w}_k(t), \dot{w}_{k+1}(t)$ transverse velocities at the k-th and $(k+1)$ - th finite element nodes, respectively
$w_\mathrm{t}(x,y,t)$ transverse displacement field due to torsion
$\dot{w}_{\mathrm{cell}}^{l,k}(t)$ transverse velocity at the (l,k) - th cell
$\dot{w}_{\mathrm{cell},1}^{l,k}(t), \dot{w}_{\mathrm{cell},2}^{l,k}(t), \dot{w}_{\mathrm{cell},3}^{l,k}(t), \dot{w}_{\mathrm{cell},4}^{l,k}(t)$ transverse velocity at the cells surrounding the (n,m) - th cell corner
$\dot{w}_\mathrm{cells}(t)$ global transverse velocity vector containing the velocities at the cell centres
x, y, z spatial coordinates
$\hat{\boldsymbol{x}}, \hat{\boldsymbol{y}}, \hat{\boldsymbol{z}}$ spatial unit vectors
$y^{l,k}$ distance in the y-direction from the (l,k) - th cell to the beam's neutral axis
δ skin depth
$\theta_x(t), \theta_y(t)$ nodal rotations in the x- and y-directions, respectively
$\theta_x(x,t)$ torsional rotation field
$\theta_{x,j}(t), \theta_{y,j}(t)$ nodal rotations in the x- and y-directions, respectively for the j-th node
$\theta_{x,k}(t), \theta_{x,k+1}(t)$ torsional rotations at the k-th and $(k+1)$ - th finite element nodes, respectively
$\dot{\theta}_{x,k}(t), \dot{\theta}_{x,k+1}(t)$ torsional angular velocities at the k-th and $(k+1)$ - th finite element nodes, respectively
μ_0 permeability of free space
ρ volumetric density of the beam material
σ electrical conductivity of the beam material
ω angular frequency

Operators

d differential operator
T transpose operator
$(\dot{\bullet})$ time derivative
$\cdot$ dot product
$\times$ cross product
-1 inverse operator
$\nabla\cdot$ divergence operator

$\nabla\times$	curl operator

Subscripts

j	finite element node index
k	finite element index aligned in the x-direction with the (l, k) - th cell

Superscripts

(l,k)	finite difference cell index
(n,m)	finite difference cell corner index

Symbols

C	arbitrary contour on the beam surface
S	surface enclosed by C

eddy current effects in a cantilever beam [8], the validation of numerical finite element results against experimental data on thin plate deflection [9], and the introduction of a novel three-dimensional finite element formulation for the computation of a nonlinear axisymmetric solenoid [10] are among the earliest studies originating from the proposed TEAM Problem 12.

Since then, numerical methods have continued to evolve. Despite being a long-standing problem, it remains a topic of current interest as research in this area continues. Numerous studies can be found that aim to reduce the number of variables to solve in various applications, such as the development of finite element methods based on the magnetic field potential to compute diverse topological shapes [11] or the use of finite difference schemes to solve eddy currents in vibrating plates subjected to time-varying magnetic fields [12,13], among many others [14–18].

However, despite the considerable progress achieved in numerical modelling techniques, the treatment of multi-physics coupling within mechanical system dynamics has historically received comparatively less attention. Traditionally, single-field problems have been predominant. However, modern engineering increasingly demands multi-physics solutions across a wide range of applications. As a result, the modelling, solution, and analysis of coupled multi-physics systems remain topics of sustained and growing interest. Examples of such couplings include fluid–structure interactions [19], magneto-hydrodynamic coupling [20], acoustic-structural coupling [21], thermoelasticity [22], aeroelasticity [23], electromechanical coupling [24], electromagnetic-structural interactions [25,26], opto-mechanical interactions [27], soil-structure interactions [28], or chemo-mechanical applications [29], among others.

Although many of these fields involve multi-physics systems and address coupling through various strategies, most commonly employing monolithic or partitioned solution approaches [30–32], the treatment of electromagnetic–mechanical coupling induced by Lorentz forces in vibrating structural systems has received limited detailed attention to date. The primary challenge lies in the difficulty of incorporating electromagnetic forces arising from eddy currents into the dynamic equations of motion of the structural system. Various approximations have been proposed to address this issue. For instance, it is common to use linear electromagnetic velocity-dependent coefficients, which are only valid for low velocities, with non-linear corrections introduced through experimental coefficients for specific designs, such as those of inertial eddy current dampers [33], or to model the electromagnetic forces in moving permanent magnets [34]. Another common approach is to propose frequency-dependent equivalent damping coefficients derived through numerical procedures and validated through experimental testing. However, these approaches often include the explicit dependence on the applied magnetic field on the electromagnetic forces in those frequency-dependent coefficients. Approximations remain prevalent in the literature, such as assuming constant [35], linear [36], or more complex frequency-dependent electromagnetic force functions [37], or simplifying the governing equations of the system by approximating certain eddy current terms [38].

Even when electromagnetic forces are obtained numerically, as in the case of a cantilever beam with eddy current damping [39], limitations still exist. In this case, calculations are restricted to the bending and torsional modes, where the prescribed modal velocities are imposed without solving the complete system response. Despite this limitation, it has been observed that bending and torsional motions, which are a priori independent, become coupled when the magnetic field is applied simultaneously in multiple directions, and only under such conditions. This bending-torsion interaction has not yet been examined in detail for vibrating structural systems subjected to magnetic fields. Moreover, owing to the restriction to modal-level analyses, the implications of this coupling on the overall structural dynamic response cannot be fully assessed, as a general formulation for addressing the electromagnetic–mechanical coupling at the system level has not been established. A similar coupling effect between nominally independent degrees of freedom has also been observed and analysed by the authors in a simple two-degree-of-freedom system, where the interaction likewise emerges exclusively under multidirectional magnetic field excitation [40].

Building upon these observations, the present work seeks to extend previous results obtained for cantilever beams and to provide a natural progression from the analysis of the simplified two-degree-of-freedom system. While beam-like structures are widely used in engineering applications and have been extensively studied in the context of structural dynamics under various external effects, such as axial loads or elastic foundations [41], the influence of multidirectional magnetic fields on the electromagnetic–mechanical coupled dynamic response requires further investigation. The primary objective is to analyse the complete dynamic behaviour of a structural beam subjected to static magnetic fields while explicitly accounting for electromagnetic–mechanical coupling, and to investigate in detail the bending-torsion interaction arising from this coupling. To this end, electromagnetic forces are explicitly incorporated into the dynamic equations of motion, enabling a comprehensive treatment of the magnetic field effects within the structural dynamics framework. Unlike previous studies, where the analysis was restricted to prescribed modal velocities or reduced-order models [39,40], the present formulation enables the solution of the fully coupled system without restricting the response to predefined modal patterns. This allows the bending-torsion interaction to emerge naturally from the governing equations and to be analysed in a general and systematic manner.

A vibrating thin, non-magnetic conductive beam subjected to a static magnetic field is studied, with self-inductance effects neglected. The structural system is modelled using finite elements, which include the degrees of freedom for bending and torsion, while the electrical problem is modelled using finite differences. Classical finite element formulations are employed for the structural system, whereas a specific recently developed finite difference method to solve eddy currents which offers adaptability and ease of implementation is employed [13,39]. This combination enables the representation of electromagnetic forces through a velocity-dependent electromagnetic damping matrix, allowing seamless integration in the beam's dynamic equations. The proposed formulation is validated against experimental results, showing good agreement in the predicted dynamic response. Consequently, two physical phenomena emerge naturally from the coupled formulation: vibration attenuation and bending-torsion coupling, the latter occurring exclusively under multidirectional magnetic excitations, in agreement with previous findings [39,40].

To thoroughly examine the beam's dynamic behaviour and assess the implications of the bending-torsion coupling, a numerical application is presented, analysing the influence of magnetic field magnitude components on the system response in both frequency and time domains. Unlike a prior study restricted to individual bending or torsional modes [39], the present work enables a system-level analysis of the coupled electromagnetic–mechanical dynamics without constraining the solution to predefined modal shapes.

The remainder of this paper is structured as follows: Section 2 details the studied system, including general problem considerations. Section 3 provides a comprehensive explanation of the numerical procedure used to obtain the electromagnetic matrix and formulate the coupled dynamic equations. In Section 4, a convergence study of the coupled electromagnetic–mechanical scheme is conducted. Section 5 presents the validation of the proposed formulation against experimental data. Subsequently, Section 6, a practical application for a particular cantilever beam is presented, with numerical results for the beam' response in both frequency and time domains. Finally, the main conclusions of this work are summarised, followed by a discussion of the current model's limitations and directions for future research.

2. System description: Beam with eddy currents

The structural system under study consists of a thin, non-magnetic conductive beam. A diagram illustrating the problem is provided in Fig. 1, corresponding to the specific case of a cantilever beam. The beam vibrates in the presence of an external, time-invariant (or static) magnetic field, denoted by $\boldsymbol{B}_{\mathrm{e}}(x,y)$. The vibration is characterised by the transverse displacement vector field $\boldsymbol{w}(x,y,t)$, while external forces are represented by $\boldsymbol{F}_{\mathrm{ext}}(x,y,t)$, where x and y represent spatial variables and t denotes time. Eddy currents, characterised by the current density vector field $\boldsymbol{J}(x,y,t)$, are induced throughout the beam's surface due to the interaction between the vibration and the magnetic field. These currents generate electromagnetic forces that mitigate the vibration, represented by the electromagnetic force density vector field $\boldsymbol{f}_{\mathrm{em}}(x,y,t)$.

The beam's geometry is defined by its length L, width b, and thickness d, aligned with the x-, y- and z-directions, respectively, where $L > b$ and $L \gg d$. The beam is considered thin and its relevant material properties include volumetric density ρ, Young's modulus E, shear modulus G, loss factor η, and electrical conductivity σ, all of which are assumed to be uniform throughout the beam and constant in time.

The external magnetic flux density vector $\boldsymbol{B}_{\mathrm{e}}(x,y)$ is given by

$$\boldsymbol{B}_{\mathrm{e}}(x,y) = B_x(x,y)\widehat{\boldsymbol{x}} + B_y(x,y)\widehat{\boldsymbol{y}} \tag{1}$$

where $B_x(x,y)$ and $B_y(x,y)$ are its scalar components in the x- and y-directions, respectively.

The vibration of the beam is described by its transverse displacement field, expressed as $\boldsymbol{w}(x,y,t) = w(x,y,t)\widehat{\boldsymbol{z}}$, where $w(x,y,t)$ denotes the transverse displacement component. In this work, $w(x,y,t)$ is assumed to

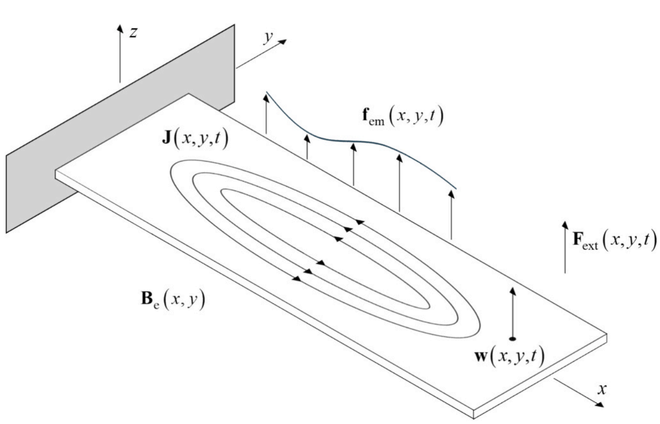

Fig. 1. Schematic representation of the electromagnetic–mechanical problem for a conductive beam.

result from the combined effects of bending and torsional vibrations, such that

$$w(x,y,t) = w_{\mathrm{b}}(x,t) + w_{\mathrm{t}}(x,y,t) \tag{2}$$

where $w_{\mathrm{b}}(x,t)$ represents the bending component, and $w_{\mathrm{t}}(x,y,t)$ accounts for the torsional contribution, defined as $w_{\mathrm{t}}(x,y,t) = \theta_x(x,t)y$, with $\theta_x(x,t)$ denoting the torsional rotation.

The interaction between the beam's vibration and the external magnetic field induces eddy currents, represented by the eddy current density vector $\boldsymbol{J}(x,y,t)$. Since the beam is thin, eddy currents are induced solely in the x-y plane, leading to

$$\boldsymbol{J}(x,y,t) = J_x(x,y,t)\widehat{\boldsymbol{x}} + J_y(x,y,t)\widehat{\boldsymbol{y}} \tag{3}$$

where $J_x(x,y,t)$ and $J_y(x,y,t)$ are the components of the eddy current density vector in the x- and y-directions, respectively. For this assumption to hold, the skin depth δ, given by

$$\delta = \sqrt{\frac{2}{\mu_0 \sigma \omega}} \tag{4}$$

where μ_0 is the permeability of free space and ω is the angular frequency of vibration, must be sufficiently large in order to satisfy $\delta > d$ [2].

The electromagnetic force density $\boldsymbol{f}_{\mathrm{em}}(x,y,t)$ caused by the induced eddy currents are given by the Lorentz force, which results in forces per unit volume given by

$$\boldsymbol{f}_{\mathrm{em}}(x,y,t) = \boldsymbol{J}(x,y,t) \times \boldsymbol{B}_{\mathrm{e}}(x,y) \tag{5}$$

where $\times$ denotes the cross product.

3. Electromagnetic-mechanical coupling forces

In this Section, the electromagnetic forces arising from the eddy currents induced in the beam are determined. The governing equations for the mechanical and electrical problems of the beam are first presented. For the mechanical problem, the general dynamic equations of motion are formulated in a finite element framework, where the electromagnetic–mechanical coupling forces due to the mechanical and electrical interactions appear as an independent term. For the electrical problem, the governing equations are established using a finite difference approach, allowing for the computation of eddy currents, which are subsequently used to determine the electromagnetic forces. These forces are then transformed from the finite difference framework into the finite element framework, resulting in general dynamics equations of motion where the electromagnetic forces are coupled.

3.1. Beam dynamic equations of motion

The beam under study, depicted in Fig. 1, is modelled using N_x one-dimensional beam-type finite elements with three degrees of freedom per node, as exemplified in Fig. 2, from which the dynamic equations of motion are subsequently derived. Each element represents a block of length h_x in the x-direction, width b in the y-direction, and thickness d in the z-direction. The j-th node incorporates bending degrees of freedom, given by the transverse displacement $w_j(t)$ and the bending rotation $\theta_{y,j}(t)$, as well as a torsional degree of freedom, represented by the torsional rotation $\theta_{x,j}(t)$. Thus, the displacement vector for the j-th node, $\boldsymbol{q}_j(t)$, is given by

$$\boldsymbol{q}_j(t) = \begin{bmatrix} w_j(t) & \theta_{x,j}(t) & \theta_{y,j}(t) \end{bmatrix}^{\mathrm{T}}, \tag{6}$$

where $[\,\bullet\,]^{\mathrm{T}}$ denotes the transpose operator. An example of the beam finite element discretisation is shown in Fig. 2, where the degrees of freedom of the j-th node are highlighted, along with the node numbering.

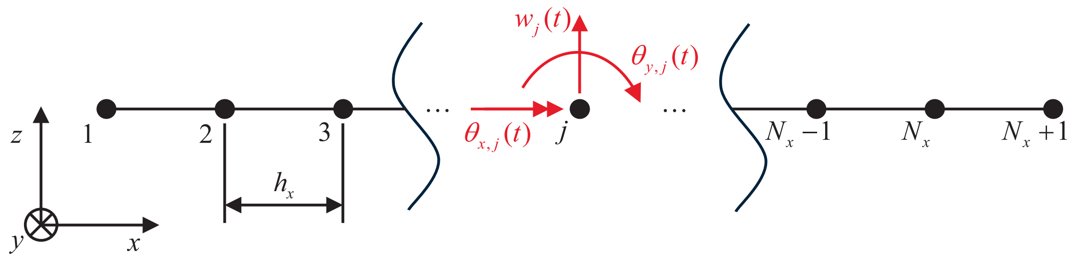

Fig. 2. Finite element discretisation.

The general dynamic equations of motion take the form

$$\boldsymbol{M}\ddot{\boldsymbol{q}}(t) + \boldsymbol{K}\boldsymbol{q}(t) = \boldsymbol{F}_{\text{ext}}(t) + \boldsymbol{F}_{\text{em}}(t) \tag{7}$$

where $\boldsymbol{M}$ is the global mass matrix, $\boldsymbol{K}$ is the global stiffness matrix, $\boldsymbol{F}_{\text{ext}}(t)$ is the vector of external nodal forces, $\boldsymbol{F}_{\text{em}}(t)$ is the vector of electromagnetic nodal forces, $(\bullet)^{\cdot}$ denotes time derivative, and $\boldsymbol{q}(t)$ is the nodal displacement vector to be determined. The global mass and stiffness matrices are assembled from their elemental counterparts, following standard formulations available in the literature [42]. Details about the displacement vector, and the assembly of the mass and stiffness matrices are provided in Appendix A.

3.2. Determination of electromagnetic forces

In the general dynamic equations of motion given in Eq. (7) the electromagnetic nodal force term, $\boldsymbol{F}_{\text{em}}(t)$, is directly associated with the induced eddy currents and is obtained from the force per unit volume, $\boldsymbol{f}_{\text{em}}(x,y,t)$, defined in Eq. (5). Eddy currents arise due to motional induction, described by the general form of Faraday's law, which in the quasi-static form [43] is given by

$$\oint_{\text{C}} \left(\frac{\boldsymbol{J}(x,y,t)}{\sigma} \right) \cdot \text{d}\boldsymbol{l} = -\int_{\text{S}} \dot{\boldsymbol{B}}_{\text{i}}(x,y,t) \cdot \text{d}\boldsymbol{S} - \int_{\text{S}} \dot{\boldsymbol{B}}_{\text{e}}(x,y) \cdot \text{d}\boldsymbol{S} + \oint_{\text{C}} \left(\dot{\boldsymbol{w}}(x,y,t) \times \boldsymbol{B}_{\text{e}}(x,y) \right) \cdot \text{d}\boldsymbol{l} \tag{8}$$

where $\boldsymbol{B}_{\text{i}}(x,y,t)$ is the magnetic flux density vector field induced by the eddy currents through self-inductance, $\dot{\boldsymbol{w}}(x,y,t)$ is the transverse velocity vector field, C is an arbitrary contour on the beam surface, S is the surfaced enclosed by C, d$\boldsymbol{l}$ is a differential length vector along C, and d$\boldsymbol{S}$ is an elementary surface area vector of S. The dot symbol $\cdot$ denotes the dot product. In this study, self-inductance effects are neglected and thus $\dot{\boldsymbol{B}}_{\text{i}}(x,y,t) = \boldsymbol{0}$, as is commonly assumed in thin conducting structures operating in low-to-moderate frequency ranges. For the beam geometries and material properties considered in this work, the electromagnetic response is expected to remain in a resistive-dominated regime, in which inductive effects associated with self-induction are secondary. A practical criterion to assess the validity of this assumption is given by the ratio between inductive and resistive effects, $\omega L_{\text{c}}/R_{\text{c}}$, where L_{c} is inductance, and R_{c} is the electrical resistance of the conductor. When $\omega L_{\text{c}}/R_{\text{c}} \ll 1$, the electromagnetic response is dominated by resistive effects and self-inductance can be neglected. For the beam and frequency range considered in this work of up to 1 kHz in Section 5, this ratio remains well below unity, confirming that the system operates in a resistive-dominated regime. This assumption is consistent with estimates available in the literature for similar configurations [3,44], which indicate that inductive contributions remain small within the frequency range considered in this work. This behaviour is also consistent with the experimental validation presented in Section 5, where the proposed model, without self-inductance, accurately reproduces the measured transmissibility curve of the beam for the higher-order modes. In addition, in this study, the displacement amplitudes are assumed to be sufficiently small for the system to be considered linear. Furthermore, $\dot{\boldsymbol{B}}_{\text{e}}(x,y) = \boldsymbol{0}$ since the magnetic field is assumed to be static. The solution of the eddy currents density $\boldsymbol{J}(x,y,t)$ from Eq. (8) enables the determination of the electromagnetic forces per unit volume $\boldsymbol{f}_{\text{em}}(x,y,t)$ via the Lorentz force from Eq. (5). However, no analytical solution exists for direct computation, necessitating numerical approaches. Thus, a numerical procedure based on finite differences is employed for this purpose and is presented first. Once the eddy currents are obtained from this numerical approach, the assembly process for determining the electromagnetic forces is described.

3.2.1. Finite differences method

An existing numerical procedure based on finite differences, adapted to the beam in Fig. 1 and expanded to include motional induction, is employed to determine the eddy currents throughout the beam surface and evaluate the Lorentz force [13,39]. In this procedure, Eq. (8) is solved for the scalar electric potential vector field $\boldsymbol{T}(x,y,t)$, defined as

$$\boldsymbol{J}(x,y,t) = \nabla \times \boldsymbol{T}(x,y,t) \tag{9}$$

with $\nabla\times$ denoting the curl operator, since, due to the principle of charge conservation, the eddy current density vector $\boldsymbol{J}(x,y,t)$ forms a solenoidal field [45]. For the currents to be induced solely in the x-y plane, as assumed by Eq. (3), the potential vector $\boldsymbol{T}(x,y,t)$ must exist only in the z-direction, i.e., $\boldsymbol{T}(x,y,t) = T(x,y,t)\hat{\boldsymbol{z}}$, where $T(x,y,t)$ is its scalar field component. Furthermore, $T(x,y,t)$ must remain constant along the edges of the beam surface [13]. This boundary condition ensures that the continuity equation, $\nabla \cdot \boldsymbol{J}(x,y,t) = 0$ where $\nabla\cdot$ denotes the divergence operator, is satisfied at the domain boundaries. Specifically, a close examination of Eq. (9) implies that for the current density to remain within the conducting surface, the tangential derivative of the electric potential along the perimeter must vanish, thereby requiring $T(x,y,t)$ to be constant along the edges. Thus, the numerical procedure solves $\boldsymbol{T}(x,y,t)$ from

$$\oint_{\text{C}} \left(\frac{\nabla \times \boldsymbol{T}(x,y,t)}{\sigma} \right) \cdot \text{d}\boldsymbol{l} = \oint_{\text{C}} \left(\dot{\boldsymbol{w}}(x,y,t) \times \boldsymbol{B}_{\text{e}}(x,y) \right) \cdot \text{d}\boldsymbol{l}. \tag{10}$$

The beam surface is discretised into N rectangular cells, with N_x cells along the x-direction and N_y cells along the y-direction. Each cell represents a rectangular block of length h_x in the x-direction, width h_y in the y-direction, and thickness d in the z-direction, within which the current density field $\boldsymbol{J}(x,y,t)$ is uniform. An example of the beam surface discretisation in the x-y plane is shown in Fig. 3, where, for the (l,k) - th cell, the current density vector $\boldsymbol{J}^{l,k}(t)$ and transverse velocity $\dot{w}^{l,k}_{\text{cell}}(t)$ of Eq. (10) are defined at each cell centre (indicated by crosses), while the electric vector potential vector $\boldsymbol{T}^{l,k}(t)$ is defined at the corners (marked with squares). The dashed line in Fig. 3 corresponds to the integral contour of Eq. (10), while the line at the centre corresponds to the beam axis and the finite elements of Fig. 2, each circle representing a finite element node.

The contour integral of Eq. (10) applied to an internal node, $T^{n,m}(t)$, results in (for more detailed information, see [13,39,46])

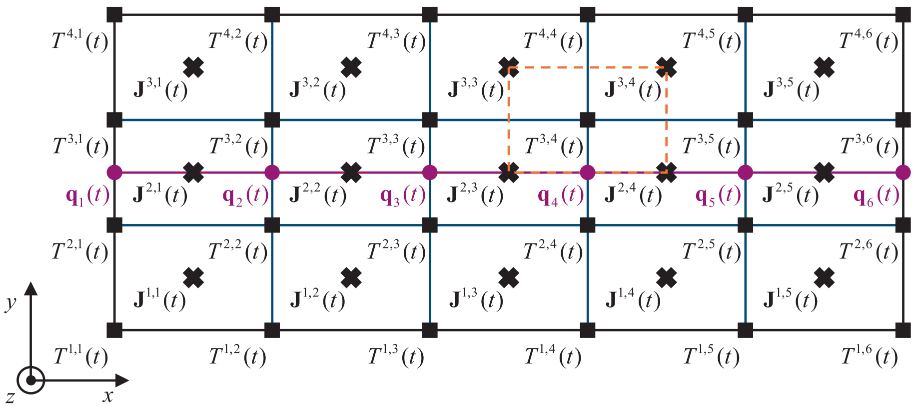

Fig. 3. Example of the discretisation of the beam surface.

$$\frac{1}{\sigma}\left[\frac{h_x}{h_y}\left(2T^{n,m}(t)-T_2^{n,m}(t)-T_4^{n,m}(t)\right)+\frac{h_y}{h_x}\left(2T^{n,m}(t)-T_1^{n,m}(t)-T_3^{n,m}(t)\right)\right]=$$
$$\frac{1}{2}\left[h_y\left(-B_{x,1}^{n,m}\dot{w}_{\text{cell},1}^{n,m}(t)+B_{x,2}^{n,m}\dot{w}_{\text{cell},2}^{n,m}(t)+B_{x,3}^{n,m}\dot{w}_{\text{cell},3}^{n,m}(t)-B_{x,4}^{n,m}\dot{w}_{\text{cell},4}^{n,m}(t)\right)+\right.$$
$$\left.h_x\left(-B_{y,1}^{n,m}\dot{w}_{\text{cell},1}^{n,m}(t)-B_{y,2}^{n,m}\dot{w}_{\text{cell},2}^{n,m}(t)+B_{y,3}^{n,m}\dot{w}_{\text{cell},3}^{n,m}(t)+B_{y,4}^{n,m}\dot{w}_{\text{cell},4}^{n,m}(t)\right)\right], \tag{11}$$

where, following the numbering scheme shown in Fig. 4 for Eq. (11), $T_1^{n,m}(t)$, $T_2^{n,m}(t)$, $T_3^{n,m}(t)$, and $T_4^{n,m}(t)$ are the potentials at each node of the five-point star centred around the potential $T^{n,m}(t)$, $\dot{w}_{\text{cell},1}^{n,m}(t)$, $\dot{w}_{\text{cell},2}^{n,m}(t)$, $\dot{w}_{\text{cell},3}^{n,m}(t)$, and $\dot{w}_{\text{cell},4}^{n,m}(t)$ are the velocities of the cells surrounding the $T^{n,m}(t)$ node, $B_{x,1}^{n,m}$, $B_{x,2}^{n,m}$, $B_{x,3}^{n,m}$, and $B_{x,4}^{n,m}$ are the analogous for the x-component of the magnetic field, and $B_{y,1}^{n,m}$, $B_{y,2}^{n,m}$, $B_{y,3}^{n,m}$, and $B_{y,4}^{n,m}$ are the analogous for the y-component of the magnetic field.. In Fig. 4, $\mathrm{d}\boldsymbol{l}_1^{n,m}$, $\mathrm{d}\boldsymbol{l}_2^{n,m}$, $\mathrm{d}\boldsymbol{l}_3^{n,m}$, and $\mathrm{d}\boldsymbol{l}_4^{n,m}$ represent the differential length vectors of each side of the dashed line for the $T^{n,m}(t)$ node.

Assembling Eq. (11) for all internal $T^{n,m}(t)$ nodes results in an indeterminate linear system of equations. However, the global vector potential $\boldsymbol{T}(t)$ can be partitioned into the edge nodes $\boldsymbol{T}_{\text{edge}}(t)$, where the potential is constant as previously mentioned, and the unknown internal nodes $\boldsymbol{T}_{\text{uk}}(t)$, i.e., $\boldsymbol{T}(t)=\begin{bmatrix}\boldsymbol{T}_{\text{edge}}(t) & \boldsymbol{T}_{\text{uk}}(t)\end{bmatrix}^{\mathrm{T}}$. In this work, for mathematical convenience, $\boldsymbol{T}_{\text{edge}}(t)$ is set to zero. Thus, a linear system of $(N_x-1)(N_y-1)$ equations is formed, resulting in

$$\boldsymbol{D}_1\boldsymbol{T}_{\text{uk}}(t)=\boldsymbol{D}_2\dot{\boldsymbol{w}}_{\text{cells}}(t) \tag{12}$$

where $\boldsymbol{D}_1$ is a symmetric coefficient matrix assembled from the left-hand side of Eq. (11), $\boldsymbol{D}_2$ is the matrix assembled from the right-hand terms of Eq. (11), and $\dot{\boldsymbol{w}}_{\text{cells}}(t)$ is the global velocity vector containing the velocities at the cell centres.

To determine the global current density vector at the centre of the cells, $\boldsymbol{J}(t)$, the definition given in Eq. (9) is used, resulting for the (l, k) - th cell in

$$J_x^{l,k}(t)=\frac{-T_1^{l,k}(t)-T_2^{l,k}(t)+T_3^{l,k}(t)+T_4^{l,k}(t)}{2h_y} \tag{13}$$

and

$$J_y^{l,k}(t)=-\frac{-T_1^{l,k}(t)+T_2^{l,k}(t)+T_3^{l,k}(t)-T_4^{l,k}(t)}{2h_x} \tag{14}$$

where $T_1^{l,k}(t)$, $T_2^{l,k}(t)$, $T_3^{l,k}(t)$, and $T_4^{l,k}(t)$ are the potentials at each of the four corners of the (l,k) - th cell, numbered in an anticlockwise manner starting from the lower left corner. The minus sign in Eq. (14) accounts for the negative arising when evaluating the y-term in Eq. (9). These equations are assembled for each of the N cells, yielding a total of $2N$ expressions. Since $T^{l,k}(t)=0$ along the beam's edge, the assembled equations result in

$$\boldsymbol{J}(t)=\boldsymbol{D}_3\boldsymbol{T}_{\text{uk}}(t) \tag{15}$$

where $\boldsymbol{D}_3$ is the coefficient matrix assembled from Eqs. (13) and (14). Finally, the Lorentz force, as defined in Eq. (5), is evaluated through integration over the volume of a cell. Since each cell represents a block of uniform current density $\boldsymbol{J}^{l,k}(t)$, this results, for the (l,k) - th cell in

$$F_{\text{em,cell}}^{l,k}(t)=h_xh_yd\left(J_x^{l,k}(t)B_y^{l,k}-J_y^{l,k}(t)B_x^{l,k}\right) \tag{16}$$

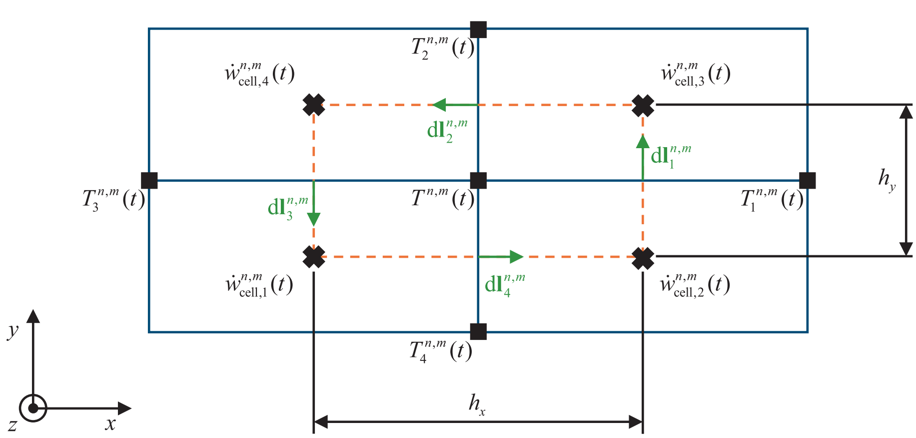

Fig. 4. Integral contour detail for the (n,m) - th internal node $T^{n,m}(t)$.

where $F^{l,k}_{\mathrm{em,cell}}(t)$ represents the Lorentz force at the (l,k) - th cell centre, acting in the z-direction, and $B^{l,k}_x$ and $B^{l,k}_y$ the magnetic field components at the (l,k) - th cell centre in the x- and y-directions, respectively. Assembly of Eq. (16) for the N cells yields

$$\boldsymbol{F}_{\mathrm{em,cells}}(t) = \boldsymbol{D}_4\boldsymbol{J}(t) \tag{17}$$

where $\boldsymbol{F}_{\mathrm{em,cells}}(t)$ is the global vector, containing the Lorentz forces at the centre of the cells, and $\boldsymbol{D}_4$ is a coefficient matrix assembled from Eq. (16). The finite difference scheme used thus allows the determination of the current density vector $\boldsymbol{J}(t)$ from the velocities at each cell, provides that Eqs. (12) and (15) are solved, and the electromagnetic forces at each cell, as indicated in Eq. (17). However, to integrate these results into the finite element framework, it is necessary to stablish the relationship between the velocities of the finite difference cells and the finite element nodes, as well as between the forces at the cells and the forces at the nodes. The corresponding procedure is explained next.

3.2.2. Finite differences and finite element transformations

To obtain the nodal forces $\boldsymbol{F}_{\mathrm{em}}(t)$ of the finite element and solve the general dynamic equations of motion in Eq. (7), two transformations are required.

First, the nodal velocities of the finite element model, $\dot{\boldsymbol{q}}(t)$, must be mapped to the velocities within the cells, $\dot{\boldsymbol{w}}_{\mathrm{cells}}(t)$, in order to evaluate Eq. (12) using the nodal velocity vector $\dot{\boldsymbol{q}}(t)$. This mapping requires the use of the definition of the transverse displacement field component, $w(x,y,t)$, given in Eq. (2). Second, the forces acting on the cells, $\boldsymbol{F}_{\mathrm{em,cells}}(t)$, must be transformed into the corresponding nodal forces of the finite element, $\boldsymbol{F}_{\mathrm{em}}(t)$.

The procedure used to perform the velocity mapping is illustrated in Fig. 5 and proceeds as follows: for any given cell (l,k), the degrees of freedom corresponding to the finite element aligned in the x-direction with this (l,k) - th cell are considered. Upon close examination of Fig. 3, it is evident that for the (l,k) - th cell, the k-th finite element meets this condition, since all cells with the same k value (i.e., the k-th column of cells) are aligned in the x-direction with the k-th finite element.

Once the degrees of freedom associated with the k-th finite element are identified, specifically, $w_k(t)$ and $\theta_{x,k}(t)$ for the left node, and $w_{k+1}(t)$ and $\theta_{x,k+1}(t)$ for the right node, these quantities are directly mapped to each side of the (l,k) - th cell (see Fig. 5). This mapping is valid because, according to Eq. (2), both $w_b(x,t)$ and $\theta_x(x,t)$ remain invariant along the y-direction. To determine the transverse velocity at the centre of the (l,k) - th cell, $\dot{w}^{l,k}_{\mathrm{cell}}(t)$, the displacements on each side of the cell are averaged and differentiated with respect to time, yielding

$$\dot{w}^{l,k}_{\mathrm{cell}}(t) = \frac{\dot{w}_k(t)+\dot{w}_{k+1}(t)}{2} + \frac{\dot{\theta}_{x,k}(t)+\dot{\theta}_{x,k+1}(t)}{2}y^{l,k} \tag{18}$$

where $y^{l,k}$ denotes the distance from the (l,k) - th cell to the beam's neutral axis.

Assembly of Eq. (18) for all N cells results in

$$\dot{\boldsymbol{w}}_{\mathrm{cells}}(t) = \boldsymbol{D}_5\dot{\boldsymbol{q}}(t) \tag{19}$$

where $\boldsymbol{D}_5$ is a coefficient matrix assembled from Eq. (18). This matrix enables the relationship between the velocity in the finite difference framework, $\dot{\boldsymbol{w}}_{\mathrm{cells}}(t)$, and the nodal velocities $\dot{\boldsymbol{q}}(t)$, in the finite element framework.

A similar reverse procedure is applied to relate the electromagnetic forces at the finite difference cells, $\boldsymbol{F}_{\mathrm{em,cells}}(t)$ in Eq. (17), to the electromagnetic forces at the finite element nodes, $\boldsymbol{F}_{\mathrm{em}}(t)$. The Lorentz force for any cell (l,k) in Eq. (16) is first decomposed into equivalent transverse forces, $F^{l,k}_{\mathrm{em,cell,1}}(t)$ and $F^{l,k}_{\mathrm{em,cell,2}}(t)$, moments in the x- direction, $M^{l,k}_{\mathrm{em,cell},x,1}(t)$ and $M^{l,k}_{\mathrm{em,cell},x,2}(t)$, and moments in the y-direction, $M^{l,k}_{\mathrm{em,cell},y,1}(t)$ and $M^{l,k}_{\mathrm{em,cell},y,2}(t)$, all located at the cell edges, as shown in Fig. 6. Here, the subscript $(\bullet)_1$ denotes the left edge, and the subscript $(\bullet)_2$ refers to the right edge of the (l,k) - th cell. The force decomposition results in

$$F^{l,k}_{\mathrm{em,cell,1}}(t) = F^{l,k}_{\mathrm{em,cell,2}}(t) = \frac{F^{l,k}_{\mathrm{em,cell}}(t)}{2} \tag{20}$$

$$M^{l,k}_{\mathrm{em,cell},x,1}(t) = M^{l,k}_{\mathrm{em,cell},x,2}(t) = \frac{F^{l,k}_{\mathrm{em,cell}}(t)y^{l,k}}{2} \tag{21}$$

and

$$M^{l,k}_{\mathrm{em,cell},y,1}(t) = -M^{l,k}_{\mathrm{em,cell},y,2}(t) = -\frac{F^{l,k}_{\mathrm{em,cell}}(t)h_x}{12} \tag{22}$$

To determine the electromagnetic nodal forces at the j-th node, $F_{\mathrm{em},j}(t)$, $M_{\mathrm{em},x,j}(t)$ and $M_{\mathrm{em},y,j}(t)$, it is necessary to sum all the contributions from the forces at the cell edges aligned in the y-direction with the j-th node. By closely inspecting Fig. 3, it is clear that only the cells with indices $(l, j-1)$ and (l,j) have force terms at the cell edges aligned with the j-th node (i.e., the $j-1$ column of cells for those to the left of the j-th node, and the j column for those to the right of the j-th node). Consequently, the resultant forces at the j-th node are given by

$$F_{\mathrm{em},j}(t) = \sum_{l=1}^{N_y}\left[F^{l,j-1}_{\mathrm{em,cell,2}}(t) + F^{l,j}_{\mathrm{em,cell,1}}(t)\right] \tag{23}$$

$$M_{\mathrm{em},x,j}(t) = \sum_{l=1}^{N_y}\left[M^{l,j-1}_{\mathrm{em,cell},x,2}(t) + M^{l,j}_{\mathrm{em,cell},x,1}(t)\right] \tag{24}$$

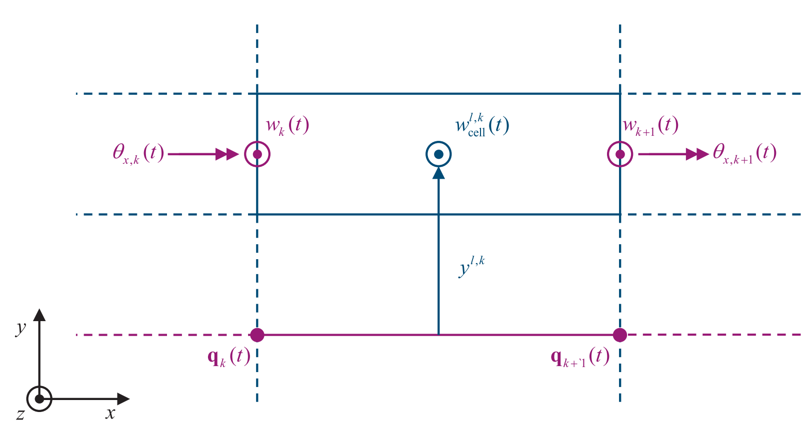

Fig. 5. Example diagram illustrating the mapping of the degrees of freedom of the k-th finite element to the (l,k) - th aligned finite difference cell associated with the k-th finite element.

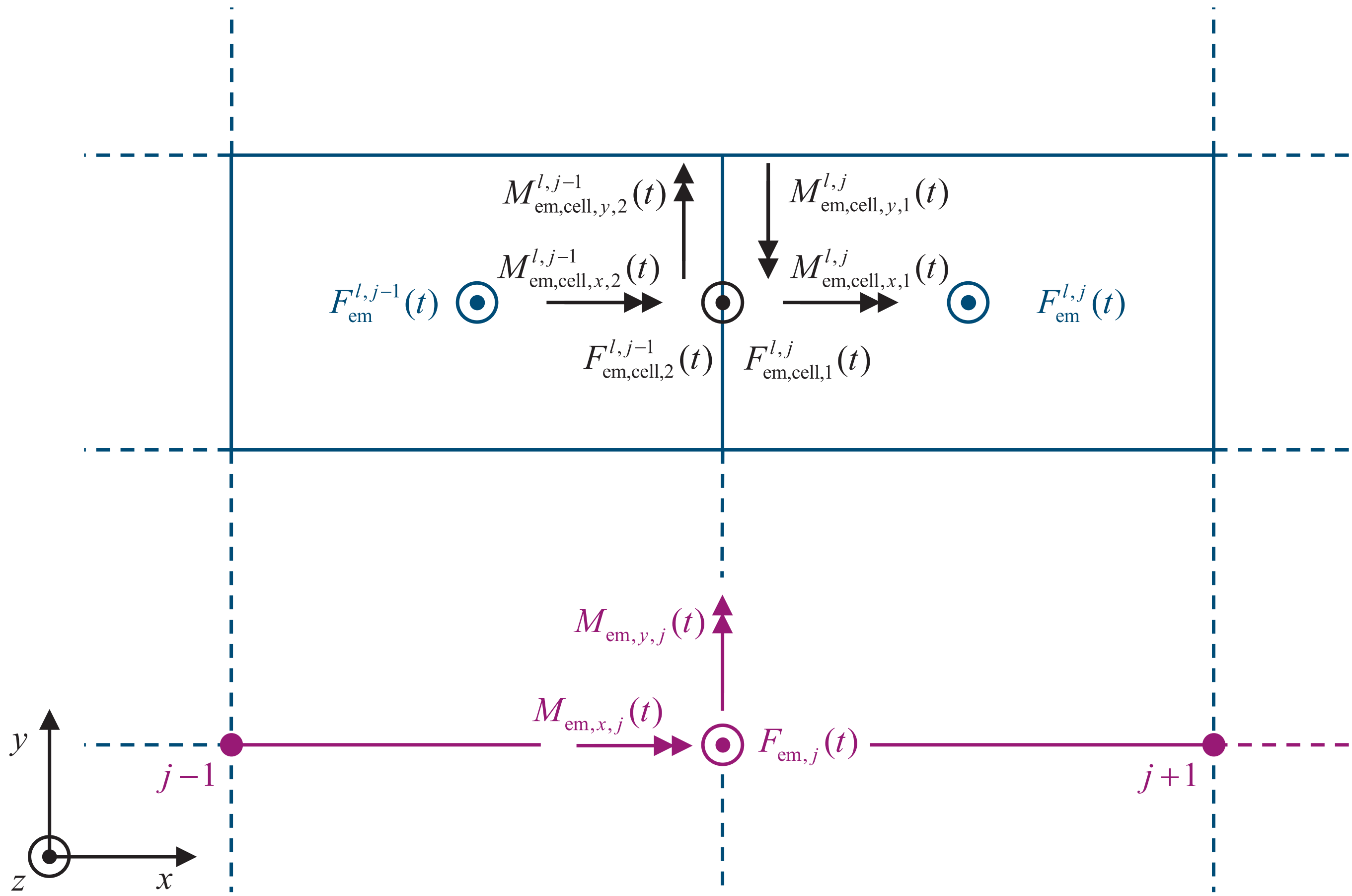

Fig. 6. Example diagram illustrating the evaluation of the summations in Eqs. (23)-(25) by highlighting the contribution of the electromagnetic forces from the l-th row to the nodal forces at the j-th node.

and

$$M_{\text{em},y,j}(t) = \sum_{l=1}^{N_y} \left[M^{l,j-1}_{\text{em,cell},y,2}(t) + M^{l,j}_{\text{em,cell},y,1}(t) \right] \tag{25}$$

In these equations, both summation terms are present for internal nodes, corresponding to the cell columns to the left and right of the j-th node. At the boundaries, however, this is not the case. For the first node ($j = 1$), there is no cell column to its left, so only the second summation term is considered. Similarly, for the last node ($j = N_x + 1$), there is no cell column to its right, and hence only the first summation term is taken into account.

An example illustrating how to evaluate the summations in Eqs. (23)-(25) is presented in Fig. 6. This figure highlights the cells in the l-th row, specifically $(l, j-1)$ and (l, j), which are aligned with the j-th node. It also shows the force decomposition terms aligned with the j-th node that contribute to the summations in Eqs. (23)-(25) for the l-th row. This procedure is repeated for all N_y rows of cells.

Assembly of Eqs. (23)-(25) for all finite element nodes results in

$$\boldsymbol{F}_{\text{em}}(t) = \boldsymbol{D}_6 \boldsymbol{F}_{\text{em,cells}}(t) \tag{26}$$

where $\boldsymbol{D}_6$ is a coefficient matrix assembled from those equations, relating the Lorentz forces $\boldsymbol{F}_{\text{em,cells}}(t)$, expressed in the finite difference framework, to the nodal forces $\boldsymbol{F}_{\text{em}}(t)$, expressed in the finite element framework.

3.2.3. Electromagnetic-mechanical coupling damping matrix

Coefficient matrices $\boldsymbol{D}_5$ and $\boldsymbol{D}_6$ have been derived to relate velocities and forces between the finite element and finite difference frameworks. These matrices, combined with those from Eqs. (12), (15), and (17), establish a direct relationship between electromagnetic forces and velocities in the finite element framework as

$$\boldsymbol{F}_{\text{em}}(t) = \boldsymbol{D}_6 \boldsymbol{D}_4 \boldsymbol{D}_3 (\boldsymbol{D}_1)^{-1} \boldsymbol{D}_2 \boldsymbol{D}_5 \dot{\boldsymbol{q}}(t) \tag{27}$$

where $(\bullet)^{-1}$ denotes the inverse operator. As previously mentioned in the definition of matrix $\boldsymbol{D}_1$ in Eq. (12), $\boldsymbol{D}_1$ is a symmetric matrix. Therefore, its explicit inversion is avoided, as this would entail a higher computational cost and reduced numerical robustness, particularly for large systems. Instead, the associated linear systems are solved directly, for instance by means of a Cholesky decomposition, which efficiently exploits the symmetric structure of $\boldsymbol{D}_1$. Matrix multiplication in Eq. (27) can then be performed straightforwardly, as all matrices involved have easily computable coefficients. A global matrix $\boldsymbol{D}_7$ is defined as

$$\boldsymbol{D}_7 = \boldsymbol{D}_6 \boldsymbol{D}_4 \boldsymbol{D}_3 (\boldsymbol{D}_1)^{-1} \boldsymbol{D}_2 \boldsymbol{D}_5 \tag{28}$$

Since $\boldsymbol{F}_{\text{em}}(t)$ in Eq. (27) depends on $\dot{\boldsymbol{q}}(t)$, it is moved to the left-hand side of Eq. (7), resulting in

$$\boldsymbol{M}\ddot{\boldsymbol{q}}(t) + \boldsymbol{C}\dot{\boldsymbol{q}}(t) + \boldsymbol{K}\boldsymbol{q}(t) = \boldsymbol{F}_{\text{ext}}(t) \tag{29}$$

where $\boldsymbol{C} = -\boldsymbol{D}_7$. Thus, the dynamic equations of motion of in Eq. (7) have been reduced to a standard second-order system of differential equations. This is a key finding, as it demonstrates that the entire effect of the eddy currents is encapsulated within the electromagnetic matrix $\boldsymbol{C}$. The resulting electromagnetic damping matrix $\boldsymbol{C}$ is symmetric and non-proportional. It contains all the information related to the electromagnetic problem and is directly responsible for the vibration damping when the beam is subjected to an external magnetic field. For both pure bending and pure torsional vibrations, an increase in the magnetic field generally leads to greater vibration attenuation. However, this matrix also exhibits an important peculiarity. When the external magnetic field is applied simultaneously in different directions, a pure bending vibration also induces torsional motion, and vice versa. In other words, a coupling effect arises between degrees of freedom associated with motions that are, a priori, independent. This coupling phenomenon is consistent with previous observations reported in a study on a cantilever beam subjected to bending or torsional modal vibrations [39], and has also been explored in a simple two-degree-of-freedom system [40]. The implications and effects of this coupling on the system response, both in the frequency and time domains, are discussed in greater detail in Section 6.

4. Convergence study

A convergence study of the fully coupled electromagnetic–mechanical formulation is carried out at the system level using the transmissibility function, which reflects the global dynamic response of the beam. This response includes the eddy-current-induced Lorentz forces mapped from the finite difference electromagnetic formulation to the finite element structural model by means of the electromagnetic damping matrix $\boldsymbol{C}$. As a result, this convergence analysis directly assesses the convergence of the coupled problem without any decoupling of the electromagnetic and structural subsystems.

The numerical transmissibility is obtained by solving the system of equations in Eq. (29) in the frequency domain for a beam subjected to harmonic base excitation with angular frequency ω. To this end, the dynamic equations of motion given in Eq. (29) are rewritten in a decoupled form as

$$\begin{bmatrix} \boldsymbol{M}_{\mathrm{bb}} & \boldsymbol{M}_{\mathrm{bu}} \\ \boldsymbol{M}_{\mathrm{ub}} & \boldsymbol{M}_{\mathrm{uu}} \end{bmatrix} \begin{Bmatrix} \ddot{\boldsymbol{q}}_{\mathrm{b}}(t) \\ \ddot{\boldsymbol{q}}_{\mathrm{u}}(t) \end{Bmatrix} + \begin{bmatrix} \boldsymbol{C}_{\mathrm{bb}} & \boldsymbol{C}_{\mathrm{bu}} \\ \boldsymbol{C}_{\mathrm{ub}} & \boldsymbol{C}_{\mathrm{uu}} \end{bmatrix} \begin{Bmatrix} \dot{\boldsymbol{q}}_{\mathrm{b}}(t) \\ \dot{\boldsymbol{q}}_{\mathrm{u}}(t) \end{Bmatrix} + \begin{bmatrix} \boldsymbol{K}_{\mathrm{bb}} & \boldsymbol{K}_{\mathrm{bu}} \\ \boldsymbol{K}_{\mathrm{ub}} & \boldsymbol{K}_{\mathrm{uu}} \end{bmatrix} \begin{Bmatrix} \boldsymbol{q}_{\mathrm{b}}(t) \\ \boldsymbol{q}_{\mathrm{u}}(t) \end{Bmatrix} = \begin{Bmatrix} \boldsymbol{F}_{\mathrm{b}}(t) \\ \boldsymbol{F}_{\mathrm{u}}(t) \end{Bmatrix} \tag{30}$$

where $\boldsymbol{q}_{\mathrm{u}}(t)$ represents the unknown displacements, $\boldsymbol{F}_{\mathrm{b}}(t)$ represents the reaction forces at the base, and $\boldsymbol{F}_{\mathrm{u}}(t)$ the harmonic external forces, which are set to zero for the convergence study. Eq. (30) thus reduces to

$$\left(-\omega^2\boldsymbol{M}_{\mathrm{uu}} + \mathrm{i}\omega\boldsymbol{C}_{\mathrm{uu}} + \boldsymbol{K}_{\mathrm{uu}}\right)\boldsymbol{Q}_{\mathrm{u}} = -\left(-\omega^2\boldsymbol{M}_{\mathrm{ub}} + \mathrm{i}\omega\boldsymbol{C}_{\mathrm{ub}} + \boldsymbol{K}_{\mathrm{ub}}\right)\boldsymbol{Q}_{\mathrm{b}} \tag{31}$$

which corresponds to the expansion of the second row in Eq.(30), where $\boldsymbol{Q}_{\mathrm{u}}$ and $\boldsymbol{Q}_{\mathrm{b}}$ are the vector amplitudes of the harmonic motions of the unknown and base displacements, respectively, and $\mathrm{i} = \sqrt{-1}$ denotes the imaginary unit.

For the convergence study, a cantilever beam made of 2024-T3 aluminium alloy is considered, adopting the geometry and material properties reported in [47], and summarised in Table 1.

For the convergence study, the magnetic field is set to $B_x = 1$ T and $B_y = 0$ T. The base displacement is defined by $\boldsymbol{Q}_{\mathrm{b}} = [w_{\mathrm{base}} \quad 0 \quad 0]^{\mathrm{T}}$, were w_{base} is the magnitude of the base displacement, and set to 1 mm.

Table 1
Geometric and material properties of the aluminium alloy 2024-T3 (data from [47]).

Property	Symbol	Unit	Value
Length	L	mm	180
Width	b	mm	9.9
Thickness	d	mm	0.404
Density	ρ	kg/m^3	2770
Young's modulus	E	GPa	66.9
Shear modulus	G	GPa	25.15
Loss factor	η	–	2.1×10^{-3}
Electrical conductivity	σ	MS/m	34.45

The system is solved numerically from Eq. (31) for frequencies ranging from 0 to 1 kHz with a frequency increment of 5 Hz. In the vicinity of resonance peaks, a refined resolution of 0.001 Hz is used to accurately capture the peak amplitudes.

The discretization is controlled by N_x and N_y. Due to the one-to-one mapping required in the coupling procedure, the longitudinal discretization N_x is kept consistent in both domains, ensuring a coherent transfer of velocity-dependent electromagnetic forces into the structural degrees of freedom.

A two-step convergence study is performed. First, N_x is fixed to 80 and N_y is progressively refined from 5 to 100 to assess the sensitivity of the coupled response to the electromagnetic grid resolution in the y-direction. Then, N_y is fixed to a converged value of 20 and N_x is refined from 60 to 250 to evaluate the convergence of the structural discretization within the same coupled framework.

Convergence is evaluated based on the modulus of the first six resonance peaks of the transmissibility function at the free end of the beam, using the finest discretization in each study as reference. Resonance frequencies are omitted from the analysis as they exhibited negligible variation across the studied mesh range, reaching convergence significantly faster than the peak modulus. A relative error below 1% is taken as the convergence criterion. The corresponding relative errors for each case are shown in Fig. 7 in a log–log representation.

The results in Fig. 7 show that the modulus of each resonance converge rapidly, with mesh-independent behaviour achieved for $N_x > 80$ and $N_y > 10$. In addition, the observed convergence curves for all cases shown in Fig. 7 exhibit nearly parallel slopes across the different modes, indicating a uniform convergence behaviour. The approximate convergence rate, estimated from the slope of these curves, is found to be approximately quadratic ($p \approx 2$), consistent with the expected accuracy of the present finite element-finite difference discretisation scheme.

5. Validation

A validation of the proposed methodology used to integrate the electromagnetic forces, $\boldsymbol{F}_{\mathrm{em}}(t)$, by means of the electromagnetic damping matrix $\boldsymbol{C}$ into the beam system shown in Fig. 1 is carried out. For that, a frequency response function in the form of a transmissibility curve is computed and compared with experimental data. This comparison validates the full coupled electromagnetic–mechanical formulation by demonstrating that the dynamic response of a physical system can be accurately reproduced.

The experimental transmissibility curve used for validation originates from the study reported by Irazu and Elejabarrieta [47], in which the dynamic response of a cantilever beam subjected to electromagnetic damping was experimentally characterised. The experimental setup, schematically illustrated in Fig. 8, consisted of an aluminium alloy 2024-T3 cantilever beam, whose geometric and material properties are summarised in Table 1, mounted on an electrodynamic shaker providing harmonic base excitation.

Electromagnetic damping was generated by placing two neodymium magnets (NdFe 35 MGOe) with dimensions 50 mm $\times$ 50 mm $\times$ 8 mm on one side of the beam, parallel to its longitudinal axis. The magnets were positioned 8 mm from the free end of the beam, with an air gap of 8 mm between the magnet surface and the beam.

The transmissibility of the system was obtained by measuring the base acceleration using a piezoelectric accelerometer operating under closed-loop control, while the beam response was measured using a laser vibrometer at a point located 5 mm from the free end. The excitation consisted of a white-noise signal covering the frequency range 0–1 kHz. Within this frequency range, the beam exhibits six vibration modes. However, due to the limited accuracy of the measurement system at very low frequencies, the first mode could not be reliably characterised during the experimental testing [47]. Consequently, the experimental

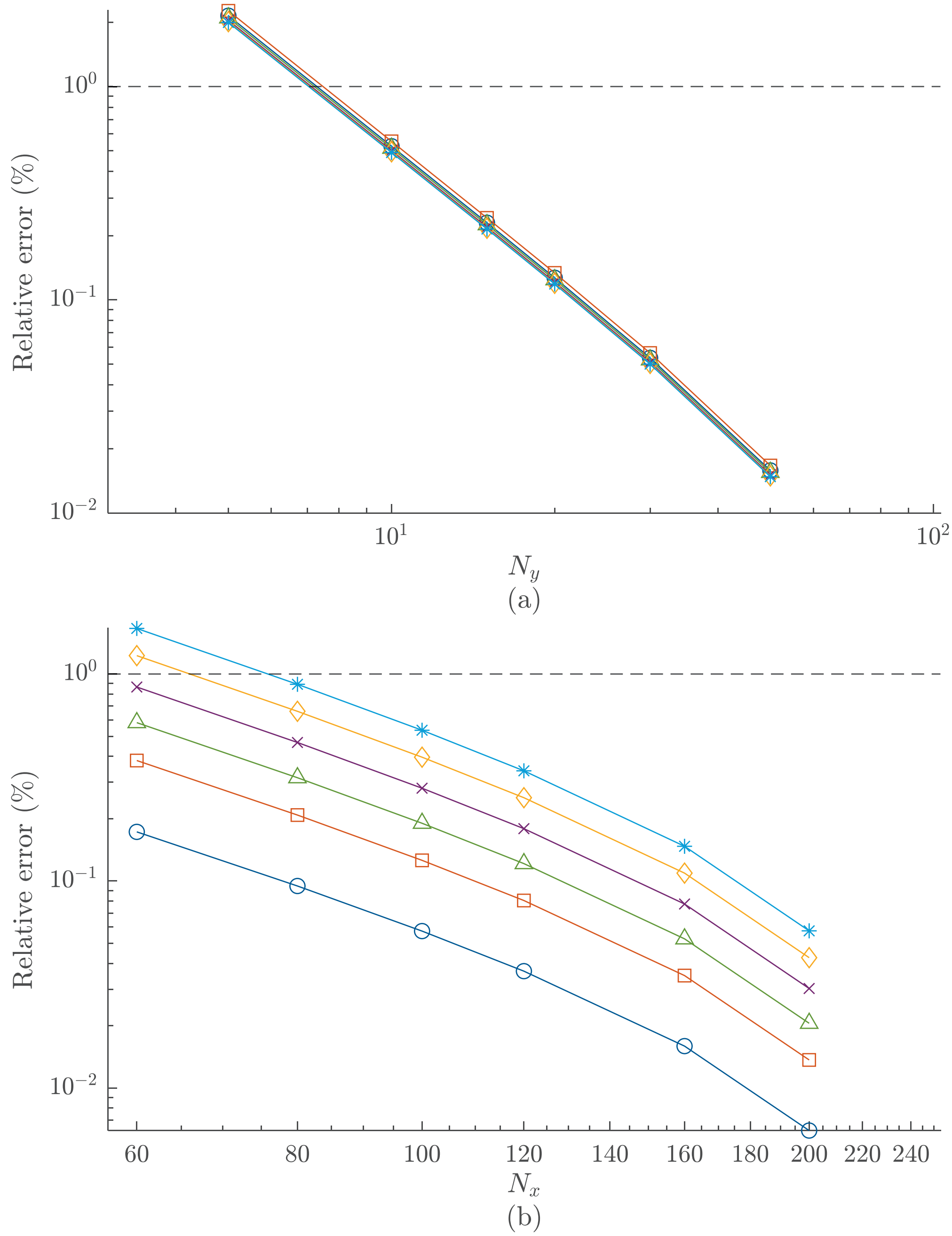

Fig. 7. Relative errors of the modulus of the first six resonance peaks: (a) N_y variation with $N_x = 80$, and (b) N_x variation with $N_y = 20$. Mode legend: mode 1 (circles), mode 2 (squares), mode 3 (triangles), mode 4 (crosses), mode 5 (diamonds), and mode 6 (asterisks). The dashed horizontal line indicates a 1% error threshold.

data used to validate the model includes only modes two to six. The transmissibility was initially acquired with a base resolution of 0.625 Hz. In order to accurately identify the resonance peaks, additional high-resolution measurements were performed locally around each mode. These refined frequency sweeps employed resolutions ranging from 0.0078 Hz for the second mode to 0.0195 Hz for the sixth mode. Further details regarding the experimental instrumentation and measurement procedure can be found in the original reference [47].

To reproduce the magnetic environment of the experiment, the spatial distribution of the magnetic flux density was obtained through a magnetostatic simulation performed using FEMM 4.2, replicating the configuration of the permanent magnets used in the experimental setup in Fig. 8. The simulation was conducted as a 2D planar problem using a mesh of 21,480 triangular elements. To ensure the accuracy of the magnetic flux distribution, the computational domain was enclosed by a far-field circular boundary with a null magnetic vector potential ($\boldsymbol{A} = \mathbf{0}$), placed sufficiently far from the magnets to prevent boundary interference. The resulting magnetic field distribution is shown in Fig. 9 (a).

According to the Lorentz force expression in Eq. (5), the $B_z(x, y)$ component provided by FEMM 4.2 only contributes to in-plane force components. These are excluded from the present beam model since they do not contribute to the electromagnetic damping in the vibration direction. The transverse component $B_y(x, y)$ is also neglected, since the magnetic field generated by the magnets is predominantly aligned with the beam axis due to their orientation, and the variation of the field across the beam width is negligible due to the relatively large width of the magnets compared to that of the beam. This is consistent with the 2D

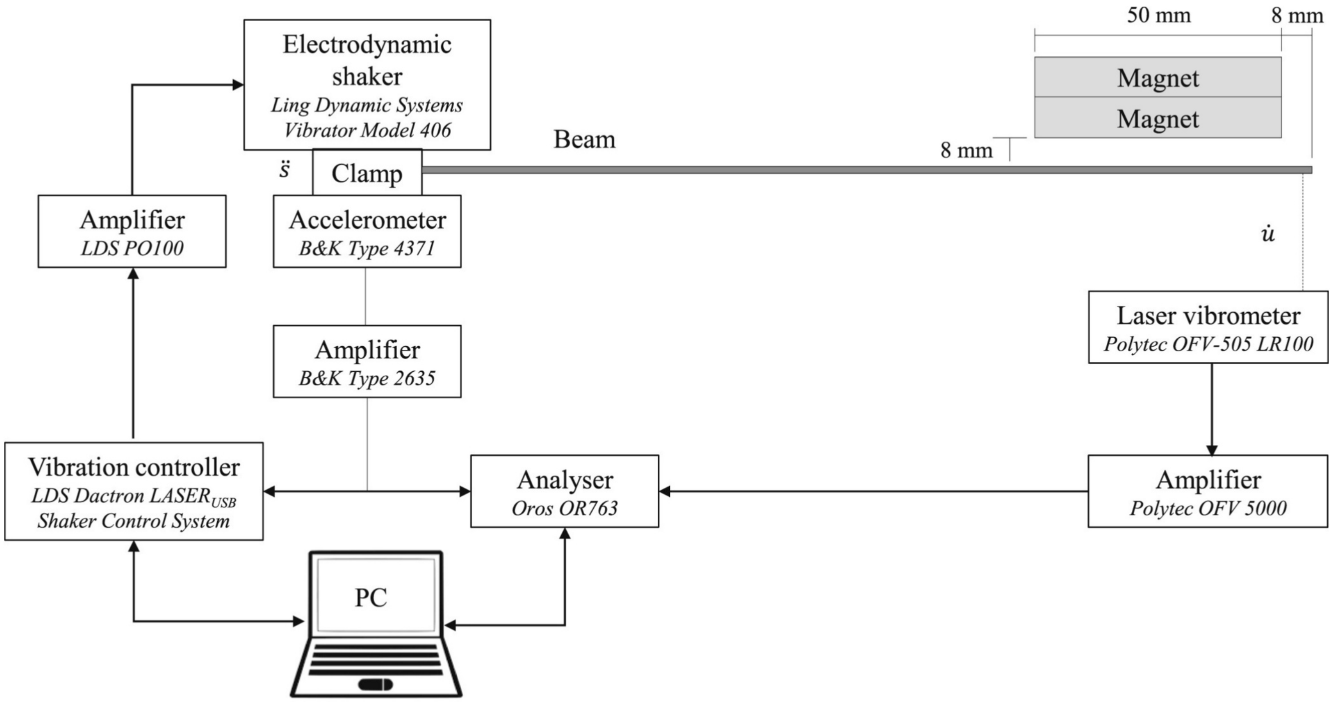

Fig. 8. Experimental setup used to obtain the transmissibility measurements (reprinted from [47], with the permission of Elsevier).

planar magnetostatic model used, where out-of-plane variations are inherently disregarded. Consequently, $B_x(x,y)$ is assumed uniform along the y-direction. Therefore, the magnetic field used in the numerical transmissibility curve is approximated by the $B_x(x,y)$ component only, whose variation along the beam axis is presented in Fig. 9(b).

The base displacement is defined by $\boldsymbol{Q}_{\mathrm{b}} = [w_{\mathrm{base}} \quad 0 \quad 0]^{\mathrm{T}}$. Since the experimental characterisation reported in [47] operates within a linear dynamic regime, an arbitrary value of $w_{\mathrm{base}} = 1$ mm is adopted in the numerical model. The system is solved numerically for frequencies ranging from 30 to 1 kHz with a frequency increment of 5 Hz. In the vicinity of resonance peaks, a refined resolution of 0.001 Hz is used to accurately capture the peak amplitudes. A discretisation of 144×21 elements is used, ensuring convergence in accordance with the results shown in Section 4.

The modulus of the experimental transmissibility curve together with the numerical prediction obtained from Eq. (31) at the measurement location (5 mm from the free end) is presented in Fig. 10. The resonance frequencies and peak transmissibility moduli obtained experimentally and numerically are compared in Table 2.

Results indicate very good agreement between the numerical and experimental transmissibility curves shown in Fig. 10. The resonance modes identified in the experimental curve are accurately reproduced by the numerical model, confirming the reliability of the coupled formulation.

As the mode number increases, a slight shift towards lower frequencies is observed in numerical results in Table 2. This small deviation suggests that the numerical model is marginally more flexible than the physical beam at higher frequencies. Possible sources of this discrepancy include uncertainties in the material properties of the aluminium alloy 2024-T3 and small deviations in the exact location of the laser measurement point. Nevertheless, the differences remain very small. The relative error in the predicted resonance frequencies remains below 1% for all identified modes, demonstrating the high accuracy of the structural model.

A strong correlation is also observed in the resonance amplitudes since the predicted and experimental amplitudes for the higher modes are in close agreement. It should be noted that the estimation of peak amplitudes at resonance is particularly sensitive to measurement noise and the frequency resolution of the experimental sweep. Despite these limitations, the logarithmic relative error of the peak transmissibility values remains below 5% for all modes listed in Table 2. This level of agreement indicates that the electromagnetic damping matrix $\boldsymbol{C}$ accurately captures the energy dissipation mechanism associated with the induced eddy currents.

Overall, the close agreement between the numerical transmissibility curve and the experimental one shown in Fig. 10, together with the quantitative values presented in Table 2, confirms the validity of the proposed formulation. In particular, the results demonstrate that the electromagnetic damping matrix $\boldsymbol{C}$ correctly represents the eddy current effects within the coupled electromagnetic–mechanical model described by Eq. (29). The proposed formulation therefore provides a reliable tool for predicting the dynamic response of structures subjected to electromagnetic damping. Moreover, the excellent agreement observed for the higher-order modes in Fig. 10 further supports the validity of the modelling assumptions, indicating that self-induction effects remain negligible within the frequency range of interest for the considered beam, since a noticeable contribution of inductive effects would have degraded the accuracy of the predicted modal behaviour.

6. Numerical application

A numerical application is developed to analyse the beam's response in both the frequency and time domains, demonstrating the effectiveness of the implemented electromagnetic damping matrix $\boldsymbol{C}$ in solving the beam's dynamic equations of motion, and more importantly, to explore the effect of the magnetic field on $\boldsymbol{C}$. First, the beam and its relevant variables are described, including its geometry, material properties, and discretisation parameters. Subsequently, practical examples are provided in both frequency and time domains, examining the influence of the external magnetic field magnitude components.

6.1. Beam model data

A cantilever beam like the one shown in Fig. 1 is chosen for the numerical application. The beam geometry and its uniform material

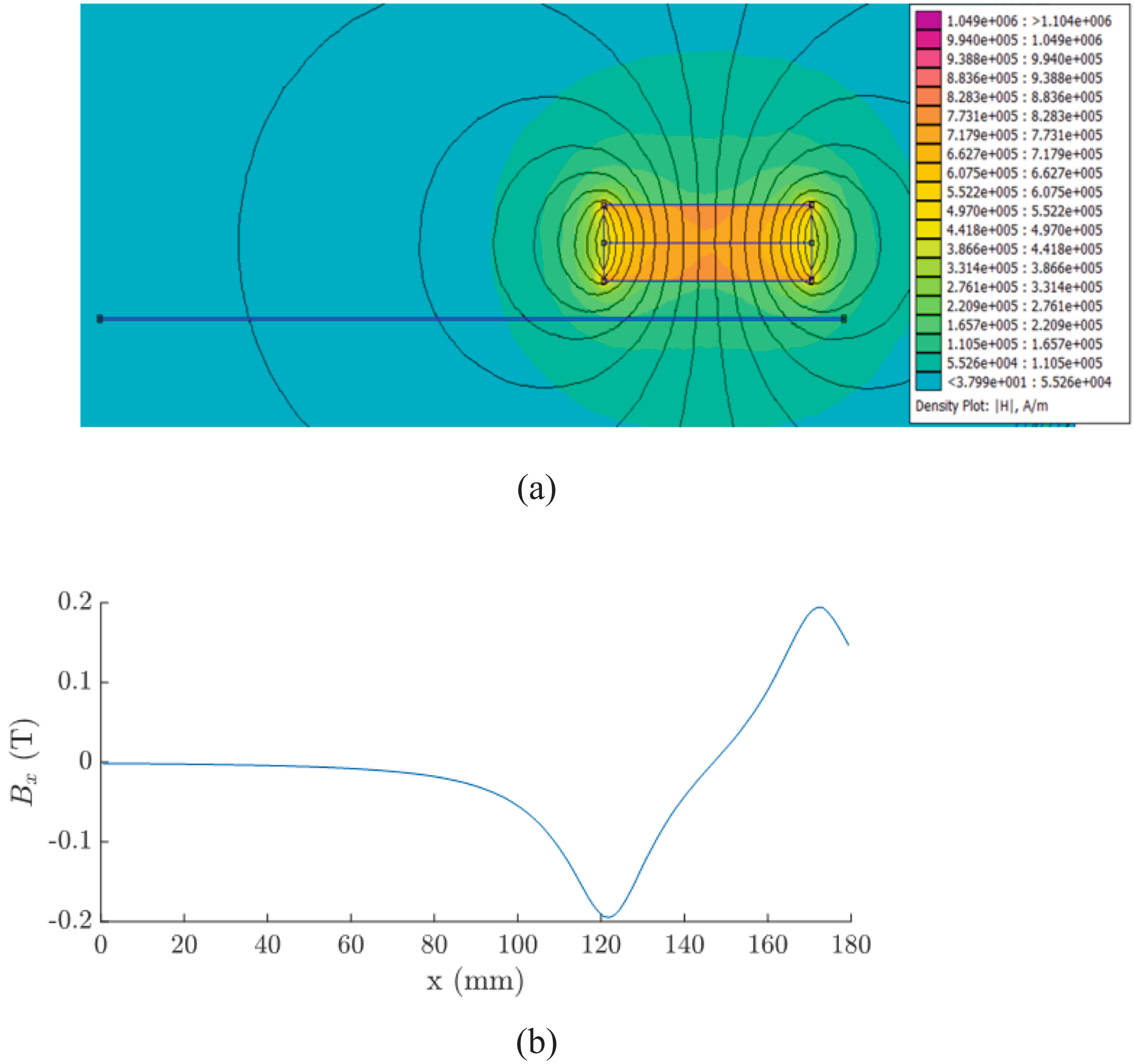

Fig. 9. Simulated magnetic field generated by the two neodymium magnets (NdFe 35 MGOe) obtained from a magnetostatic simulation in FEMM 4.2: (a) spatial distribution of the magnetic flux density magnitude; (b) variation of the $B_x(x, y)$ component along the beam axis.

properties are summarised in Table 3. Aluminium, a non-magnetic conductive material known for its high conductivity, is selected for the study.

The beam is discretised using 121 finite elements along the x-direction. For the finite difference scheme, 21 rectangular cells are employed along the y-direction. These discretisation levels are chosen to ensure converged and mesh-independent results, based on the convergence results shown in Section 4.

Different magnitudes of the magnetic field components are explored to assess how increasing field magnitude influences the results. The external magnetic field is applied in the x- and y-directions. For both frequency- and time-domain analyses, the two cases listed in Table 4 are considered. It is important to note that these two cases focus exclusively on the response of the beam when subjected to multidirectional magnetic fields. The effect of a unidirectional magnetic field is not examined here, since the present study is specifically concerned with analysing the coupling that arises between bending and torsional motions in the system response. This coupling only manifests when the magnetic field is multidirectional. Moreover, it is already well established that, for a beam of this type, applying the magnetic field in a single direction does not induce any coupling between bending and torsion, and the effects of unidirectional fields of varying magnitudes on the system response have been thoroughly investigated in previous work [39].

6.2. Frequency-domain analysis – Harmonic base displacements

For the cases presented in Table 4, a harmonic base displacement of amplitude $\boldsymbol{Q}_\mathrm{b} = [w_\mathrm{base} \quad 0 \quad 0]^\mathrm{T}$ is applied, with $w_\mathrm{base} = 1$ mm, a sufficiently small amplitude to ensure linear behaviour, at a frequency $f = \omega/(2\pi)$. The transmissibility curves between the free-end degrees of freedom and the base displacement are obtained from Eq. (31). The system is solved for frequencies ranging from 0 Hz to 400 Hz, with a frequency resolution of 5 Hz, except around the resonance peaks, where a finer resolution of 0.001 Hz is used to capture the detailed behaviour.

Case 1.

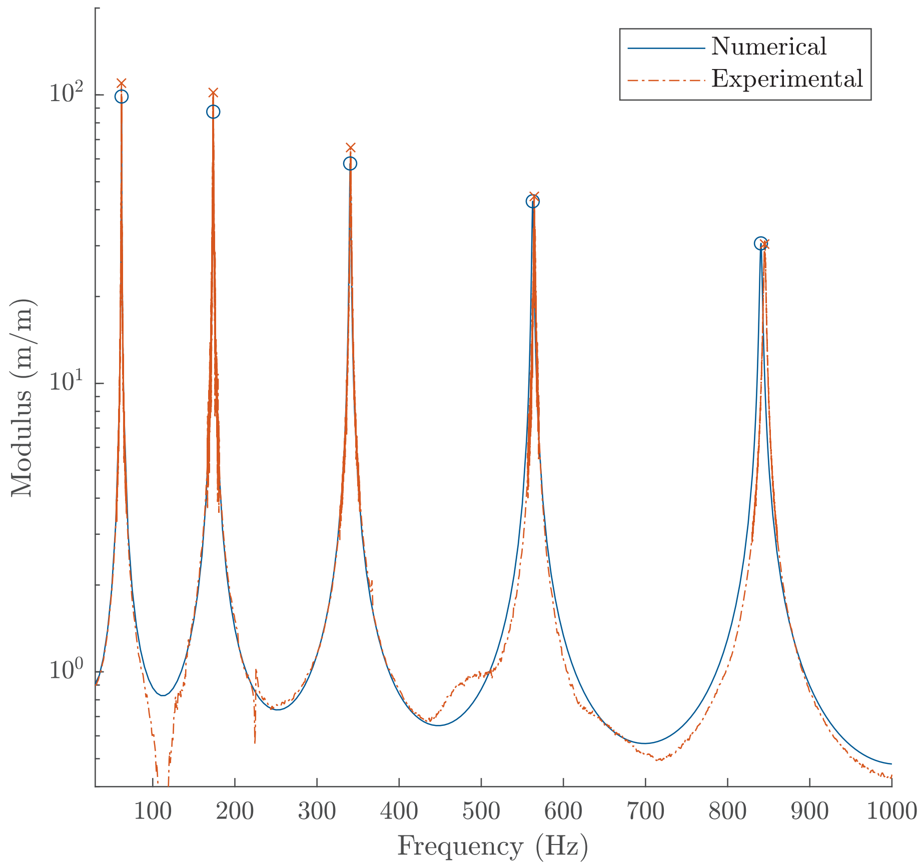

Fig. 10. Experimental [47] and numerical transmissibility modulus for the cantilever beam measured at a point located 5 mm from the free end. Symbols indicate the resonance peaks for the numerical curve (circles), and the experimental curve (crosses).

Table 2
Comparison between experimental [47] and numerical resonance frequencies and peak transmissibility amplitudes.

	Frequency (Hz)		Modulus (m/m)	
Mode	Experimental	Numerical	Experimental	Numerical
2	61.9	62.04	109.9	98.7
3	173.7	173.7	101.9	87.4
4	341.0	340.4	65.7	57.8
5	564.6	562.7	44.5	42.8
6	845.1	840.6	30.4	30.6

Table 3
Beam geometry and material properties.

Property	Symbol	Unit	Value
Length	L	mm	200
Width	b	mm	25
Thickness	d	mm	1
Volumetric density	ρ	kg/m^3	2700
Young's modulus	E	GPa	65
Shear modulus	G	GPa	25
Electrical conductivity	σ	MS/m	35

Table 4
Scenarios analysed in both the frequency and time domains.

	B_x (T)	B_y (T)
Case 1	0.1, 0.2, 0.3	0.1
Case 2	0.1	0.1, 0.2, 0.3

In this case, the response of the cantilever beam is studied as a function of the magnetic field component B_x, while keeping B_y constant at 0.1 T, as specified in Table 4. Specifically, the modulus of the transmissibility curves is analysed between the transverse displacement at the free end and the base displacement, and between the torsional rotation at the free end and the base displacement. The results obtained are presented in Figs. 11 and 12.

From the transmissibility curves in Figs. 11 and 12, the following observations can be made:

- Three distinct resonance peaks at 19.8 Hz, 124.2 Hz, and 347.7 Hz are observed in the transverse displacement transmissibility curves shown in Fig. 11, corresponding to the first three bending modes.

  As the magnetic field increases in magnitude, the resonance peaks decrease significantly, indicating enhanced damping. Specifically, the first, second, and third modes are attenuated by approximately 89% as B_x increases from 0.1 T to 0.3 T. This suggests that the damping effect is mode-independent for bending modes.

  Outside of the resonance peaks and in their vicinity, the modulus of the transmissibility curves in Fig. 11 remains largely unchanged regardless of the magnetic field magnitude.

- Coupling between bending and torsional modes is evident, as the torsional transmissibility curve in Fig. 12 remains non-zero across the frequency range. This coupling originates from the nature of the electromagnetic damping matrix $\boldsymbol{C}$, which is inherently non-proportional. Specifically, the off-diagonal terms of $\boldsymbol{C}$, which are responsible for the interaction between bending and torsional degrees of freedom, only arise when the magnetic field has components in multiple directions [39]. In simplified systems, such off-diagonal terms have been shown to scale with the product B_xB_y [40],

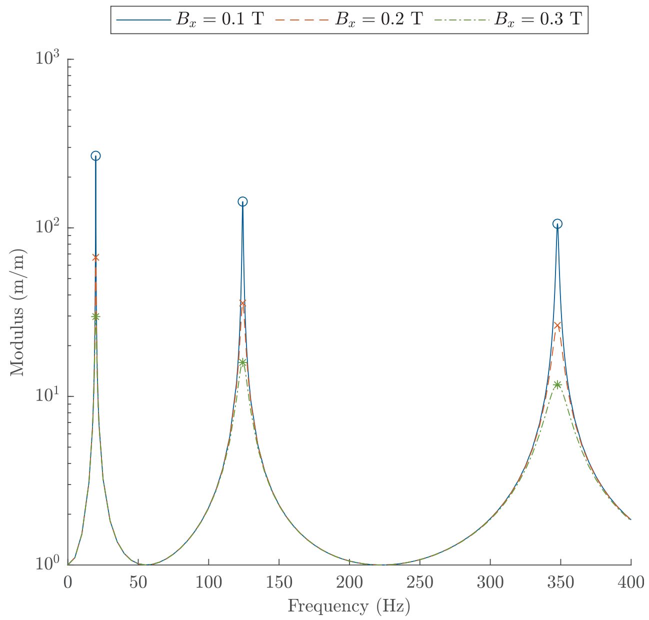

Fig. 11. Modulus of the transmissibility curves (m/m) between the transverse displacement at the free end of the beam and the base displacement, highlighting the resonance peaks for different values of B_x with B_y fixed at 0.1 T. The circles denote the maxima for $B_x = 0.1$ T (solid line), the crosses indicate the maxima for $B_x = 0.2$ T (dashed line), and the asterisks mark the maxima for $B_x = 0.3$ T (dash-dot line).

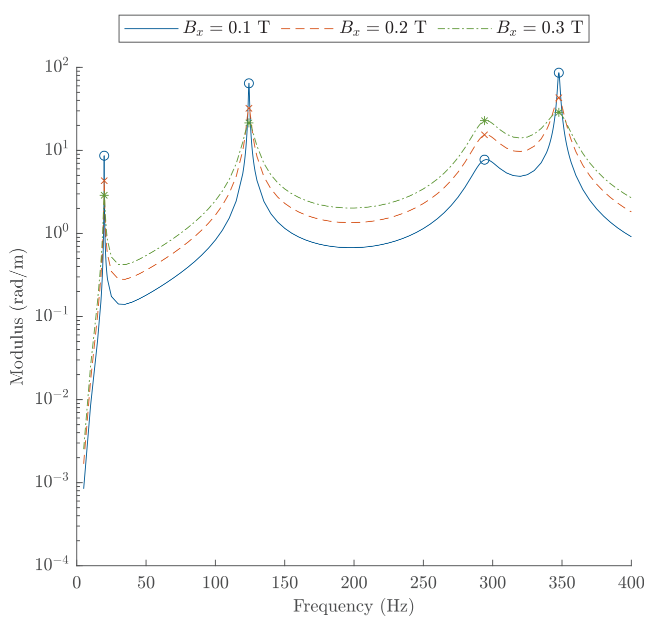

Fig. 12. Modulus of the transmissibility curves (rad/m) between the torsional rotation at the free end of the beam and the base displacement, highlighting the resonance peaks for different values of B_x, with B_y fixed at 0.1 T. The circles denote the maxima for $B_x = 0.1$ T (solid line), the crosses indicate the maxima for $B_x = 0.2$ T (dashed line), and the asterisks mark the maxima for $B_x = 0.3$ T (dash-dot line).

illustrating that they vanish when the field is applied along a single direction. Accordingly, for unidirectional magnetic fields, the formulation leads to a diagonal damping matrix and no coupling between bending and torsional motions is observed [39,40]. In that case, consequently, the torsional transmissibility curve in Fig. 12 would remain identically zero over the full frequency range.

- The coupled torsional transmissibility shown in Fig. 12 presents the same three resonance peaks as in Fig. 11, corresponding to bending modes, as well as an additional peak at 294.1 Hz, associated with the first torsional mode.

  The bending peaks in Fig. 12 behave similarly to those in Fig. 11, decreasing in amplitude with increasing B_x. Specifically, these peaks are reduced by approximately 67%. However, the torsional peak exhibits the opposite trend, increasing in magnitude by 194.84% from 0.1 T to 0.3 T. This contrasting peak behaviour, previously observed in a simplified two-degree-of-freedom system [40], is again attributed to the non-proportional nature of the electromagnetic damping matrix $\boldsymbol{C}$.

  Outside the resonance peaks and in their vicinity, the modulus of the transmissibility curves in Fig. 12 increases with the magnetic field.

Case 2.

In this case, the cantilever beam's response is examined with respect to variations in the magnetic field component B_y, while maintaining B_x fixed at 0.1 T, as indicated in Table 4. The analysis focuses on the modulus of the transmissibility curves between the transverse displacement at the free end and the base displacement, as well as between the torsional rotation at the free end and the base displacement. The corresponding results are shown in Figs. 13 and 14.

From Figs. 13 and 14 the following can be deduced:

- In contrast to Case 1, the transmissibility curves in Fig. 13 remain unchanged as the magnetic field magnitude increases, indicating that variations in B_y do not affect damping in the bending modes. Hence, only B_x contributes to the damping of transverse displacement.
- Coupling between bending and torsional degrees of freedom is again observed, as evidenced by the non-zero torsional transmissibility in Fig. 14, due to the magnetic field being applied in multiple directions, as in Case 1.
- The modulus of the transmissibility shown in Fig. 14 increases with B_y, except at the torsional resonance peak, which is attenuated as the

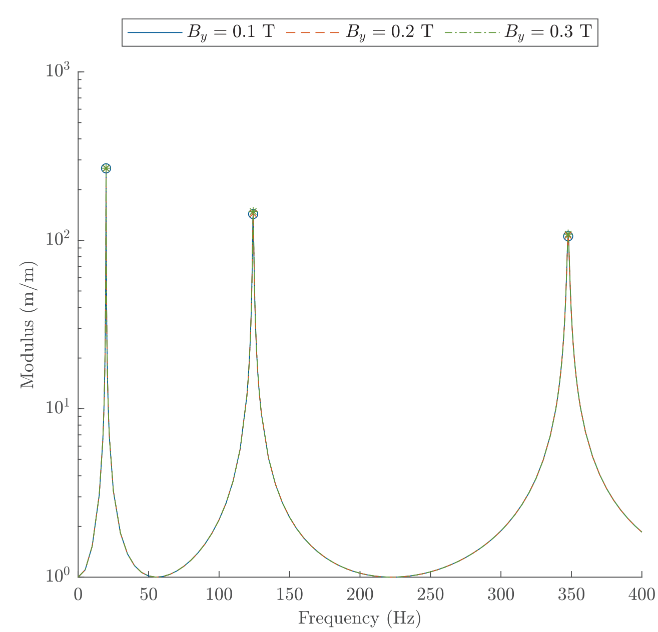

Fig. 13. Modulus of the transmissibility curves (m/m) between the transverse displacement at the free end of the beam and the base displacement, highlighting the resonance peaks for different values of B_y, with B_x fixed at 0.1 T. The circles denote the maxima for $B_y = 0.1$ T (solid line), the crosses indicate the maxima for $B_y = 0.2$ T (dashed line), and the asterisks mark the maxima for $B_y = 0.3$ T (dash-dot line).

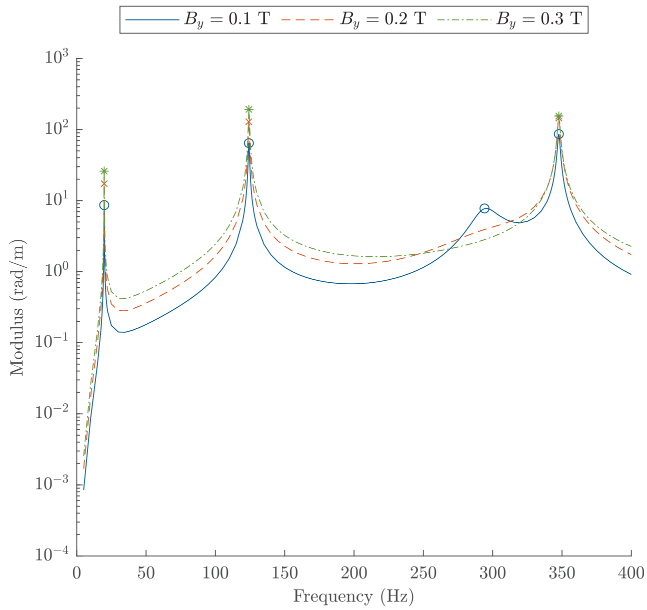

Fig. 14. Modulus of the transmissibility curves (rad/m) between the torsional rotation at the free end of the beam and the base displacement, highlighting the resonance peaks for different values of B_y, with B_x fixed at 0.1 T. The circles denote the maxima for $B_y = 0.1$ T (solid line), the crosses indicate the maxima for $B_y = 0.2$ T (dashed line), and the asterisks mark the maxima for $B_y = 0.3$ T (dash-dot line).

magnetic field increases and disappears entirely for 0.2 T and 0.3 T. This behaviour is attributed to the non-proportional nature of $\boldsymbol{C}$. The increase in transmissibility modulus is not uniform across the frequency range, with the three bending peaks increasing by 200.3%, 198.1%, and 79,3%, respectively.

These findings, alongside those from Case 1, demonstrate that simultaneous attenuation of both bending and torsional vibrations cannot be achieved when magnetic fields are applied in multiple directions. The inability to simultaneously attenuate both bending and torsional vibrations can be interpreted in terms of energy redistribution between the coupled modes. The Lorentz forces induced by the eddy currents depend on the velocity field, and when a magnetic field is applied in multiple directions simultaneously, they are not aligned with a single deformation pattern. As a result, part of the mechanical energy associated with one mode is effectively redirected towards the other. While the total energy of the system is dissipated through electromagnetic damping effects, this redistribution implies that enhancing the attenuation of one mode may lead to increased participation of the other. Consequently, a trade-off arises, whereby simultaneous attenuation of both bending and torsional responses cannot be achieved. This behaviour is consistent with the energy exchanged mechanisms observed in a simplified two-degree-of-freedom system subjected to electromagnetic damping [40]. The coupling effect inherent to this system may yield counterintuitive responses, as observed, for example, in Case 2: while torsional vibrations appear attenuated for higher magnetic field magnitudes, the damping in bending modes is reduced – and conversely, in Case 1, increased damping in the bending modes is accompanied by less attenuation of the torsional mode.

Equivalent findings to those observed in this frequency-domain analysis were previously identified in a simplified two-degree-of-freedom system, where coupling between the two degrees of freedom was only apparent when the magnetic field was applied simultaneously in the directions associated with both degrees of freedom. Similarly to the results presented here, increasing the magnetic field in one direction, while keeping it fixed in the other, led to enhance attenuation in one degree of freedom but a reduction in the other, and vice versa. However, as in the present cantilever beam study, simultaneous enhancement of attenuation in both degrees of freedom was never observed [40].

6.3. Time-domain analysis – Transient response to an initial deformation

The objective of the time-domain analysis, as with the frequency-domain study, is to investigate the influence of the magnitude of the magnetic field components on the transient response of the cantilever beam under consideration. To this end, the transient responses of the transverse displacement and the torsional rotation at the free end of the beam are analysed. The study cases considered are the same as those in the frequency-domain analysis and are summarised in Table 4.

An initial deformation is applied to the cantilever beam, corresponding to the deflection produced by the static response to a point load at the free end. Therefore, there is no initial torsional rotation, i.e., $\theta_x(x,0) = 0$, and the initial bending deformation is given by $w(x,0)$ and $\theta_y(x,0)$ as [48]

$$w(x,0) = w_{\max}\frac{x^2}{2L^2}\left(3-\frac{x}{L}\right) \tag{32}$$

and

$$\theta_y(x,0) = w_{\max}\frac{3x}{2L^2}\left(2-\frac{x}{L}\right) \tag{33}$$

where $w_{\max}$ represents the maximum deflection, which is set to $w_{\max} = 1$ mm in the numerical application. To analyse the dynamic response of the cantilever beam to this initial deformation, the well-known Newmark method is applied directly to Eq. (29). While alternative time-integration algorithms, such as Wilson-θ or Houbolt, could also be used to solve the system and would reproduce comparable results, the Newmark method has been chosen due to its widespread adoption, its unconditional stability for typical parameter choices ($\alpha = 0.25$, $\beta = 0.5$), and its proven accuracy for structural dynamic problems [49]. In this study, no external forces are applied, thus,$\boldsymbol{F}_{\text{ext}}(t) = \boldsymbol{0}$, and that the initial conditions are given by $\dot{\boldsymbol{q}}(0) = \boldsymbol{0}$ and $\boldsymbol{q}(0)$ is determined by the initial deflection, with $\boldsymbol{q}_j(0) = \left\{ w(x_j,0) \quad 0 \quad \theta_y(x_j,0) \right\}^{\mathrm{T}}$, where x_j denotes the x-coordinate of the j-th node.

The Newmark integration coefficients are set to $\alpha = 0.25$ and $\beta = 0.5$. Further details on the Newmark method can be found extensively in the literature [49], and its specific implementation is described in Appendix B.

For the different cases presented in Table 4, the dynamic response of the cantilever beam is computed from $t = 0$ s to $t = 1$ s, using a time step of $\Delta t = 0.001$ s. In all cases, the time response of the free-end degrees of freedom of the cantilever beam is analysed.

Case 1.

In this case, the transient response of the cantilever beam is examined as a function of the magnetic field component B_x, while B_y is held constant at 0.1 T, as detailed in Table 4. The analysis focuses on the time evolution of the transverse displacement at the free end of the beam, $w_L(t)$, and the torsional rotation at the free end of the beam, $\theta_{x,L}(t)$ The results are shown in Figs. 15 and 16.

From the time-domain response, it can be observed that:

- The transverse displacement time response in Fig. 15 shows that increasing B_x results in faster convergence to steady state and reduced amplitude in the steady-state oscillations. This confirms enhanced damping as the magnetic field magnitude increases.
- Similarly to the frequency-domain results, the presence of coupling between bending and torsion is revealed by the non-zero torsional response observed in Fig. 16.
- The overall behaviour of the transient response of the torsional rotation shown in Fig. 16 is similar to that of the transverse displacement response in Fig. 15, as the influence of increasing B_x on

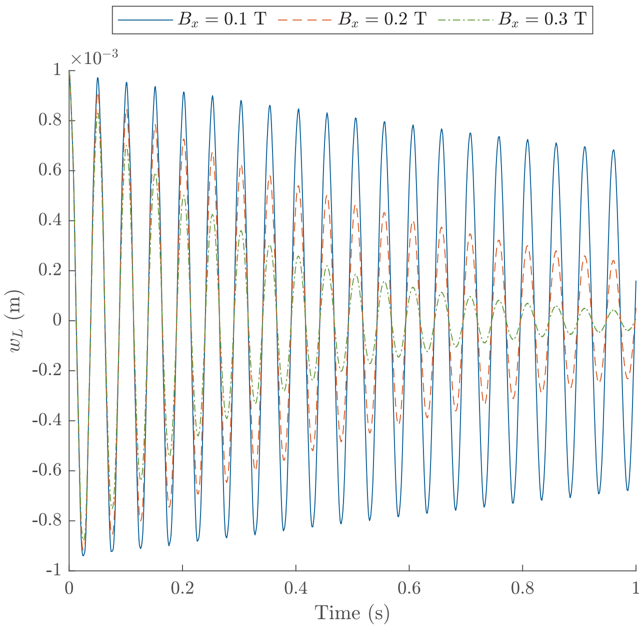

Fig. 15. Time response of the transverse displacement at the free end of the beam, $w_L(t)$, for Case 1. The solid, dashed, and dash-dot lines correspond to $B_x = 0.1$ T, $B_x = 0.2$ T, and $B_x = 0.3$ T, respectively. In all cases, B_y is fixed at 0.1 T.

torsional damping can be clearly observed in how quickly the response reaches steady state: the higher the value of B_x, the sooner the steady state is achieved and the more rapidly the oscillations decay. However, unlike the transverse displacement response in Fig. 15, the initial stage of the torsional rotation response exhibits oscillations of greater amplitude as B_x increases, despite the system still reaching the steady state earlier.

This initial transient effect reflects the contribution of higher-order modes to the coupled torsional motion. Since the initial deformation applied to the beam closely resembles the first bending mode, higher-order modes are not significantly visible in the transverse displacement responses shown in Fig. 15. However, their contribution is apparent in the torsional responses in Fig. 16 and further clarified by the spectrograms in Fig. 17.

Although Fig. 16 shows a coupled torsional motion, the response is dominated by bending modes, particularly the first one. As shown in Fig. 17, this mode exhibits higher spectral energy as B_x increases but also attenuates more rapidly. Other bending modes are also significant initially, though to a lesser extent, and they tend to diminish over time, a process that accelerates with higher B_x values. Interestingly, Fig. 17 reveals that despite Fig. 16 depicting torsional motion, the first torsional mode has a smaller impact on the overall response. However, this mode exhibits the opposite behaviour to the bending ones: as B_x increases, its spectral contribution grows and it persists longer over time. This contrasting behaviour between bending and torsional modes is consistent with the frequency analysis for Case 1 previously shown in Fig. 12.

Case 2.

Here, the transient behaviour of the cantilever beam is examined with respect to variations in the magnetic field component B_y, while keeping B_x fixed at 0.1 T, as listed in Table 4. As in Case 1, the analysis considers the time-domain responses of the transverse displacement $w_L(t)$ and the torsional rotation $\theta_{x,L}(t)$ at the free end of the beam. The corresponding results are presented in Figs. 18 and 19.

From the time-domain responses, the following observations can be made:

- The transverse displacement response in Fig. 18 is unaffected by variations in B_y. Despite the observed attenuation over time, the

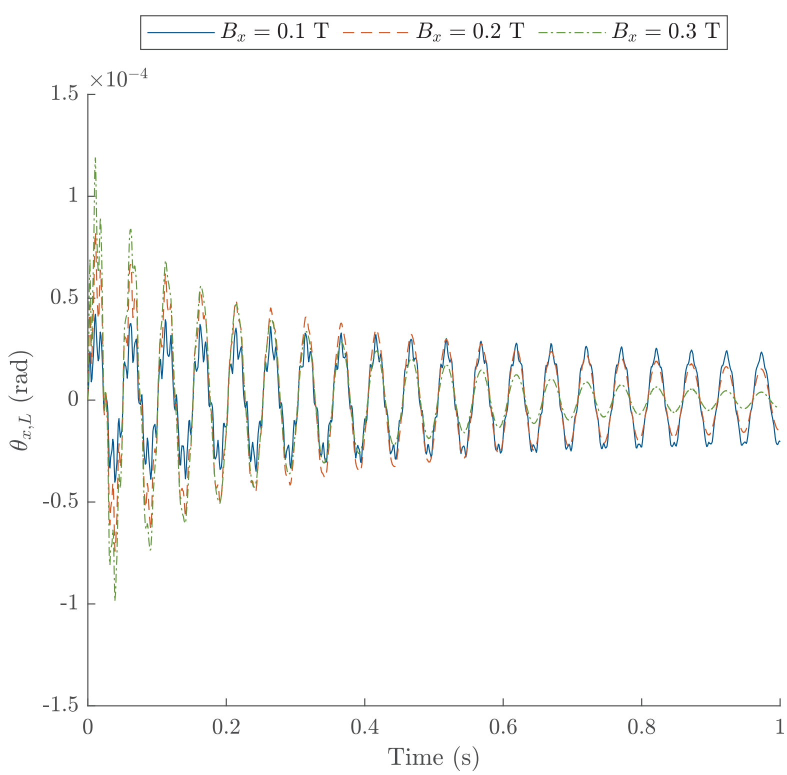

Fig. 16. Time response of the torsional rotation at the free end of the beam, $\theta_{x,L}(t)$, for Case 1. The solid, dashed, and dash-dot lines correspond to $B_x = 0.1$ T, $B_x = 0.2$ T, and $B_x = 0.3$ T, respectively. In all cases, B_y is fixed at 0.1 T.

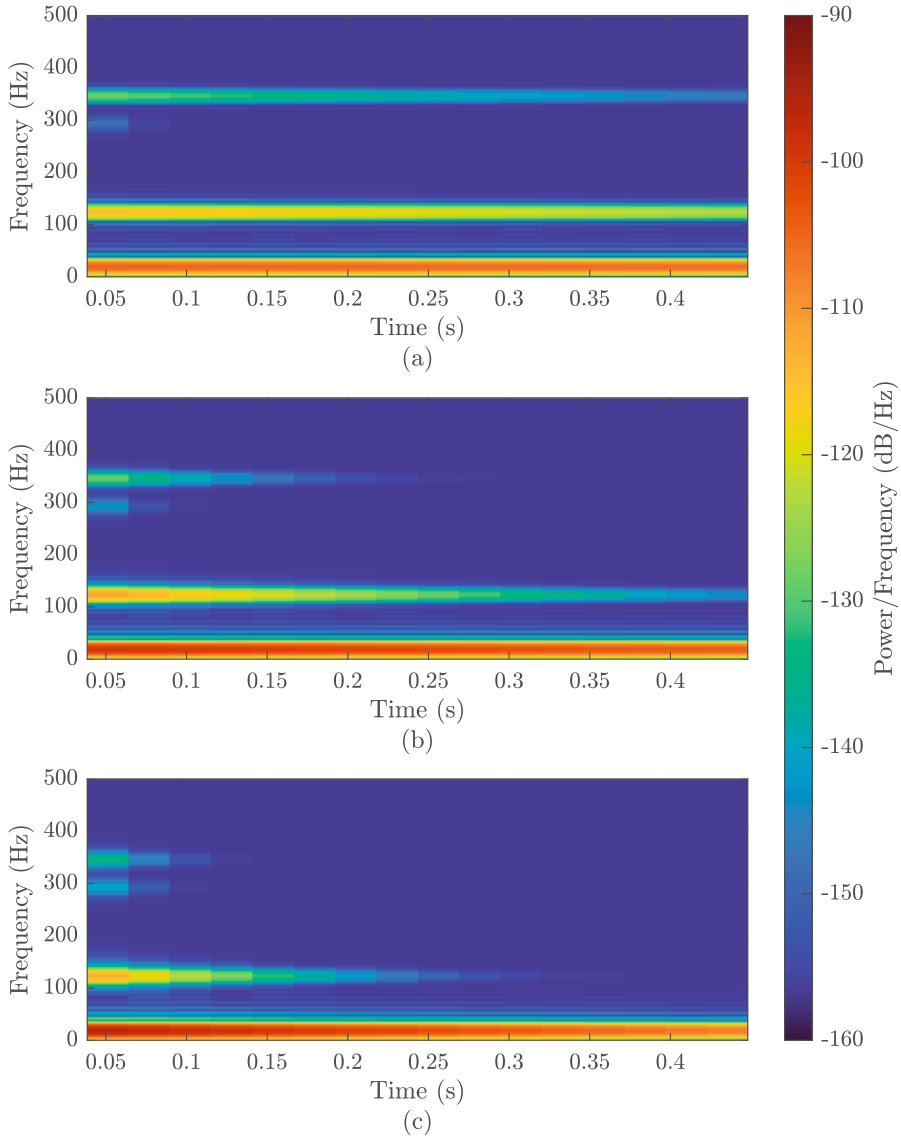

Fig. 17. Spectrograms of the torsional response for Case 1: (a) $B_x = 0.1$ T, (b) $B_x = 0.2$ T, and (c) $B_x = 0.3$ T.

damping rate remains unchanged, confirming that B_y has a negligible effect on this degree of freedom. The attenuation observed is instead due to the presence of B_x, which remains constant across all three instances, resulting in the same damping rate.

- Coupling between the vibration modes persists, as seen by the non-zero torsional response in Fig. 19.

In contrast, the torsional rotation response shown in Fig. 19 increases in amplitude at the steady state and exhibits slower decay as B_y increases. As in Case 1, the noise observed in the initial torsional oscillations is attributed to the contribution of higher-order modes, as can be clearly seen in the spectrograms shown in Fig. 20.

As in the previous case, despite depicting a coupled torsional motion in Fig. 19, Fig. 20 shows that the response is dominated by bending modes, especially the first one, as expected, given the applied initial deformation. However, unlike Case 1, the opposite behaviour is observed between modes: the bending modes increase their spectral contribution with B_y and attenuate more slowly, while the first torsional mode attenuates very rapidly, eventually disappearing for high values of B_y. Consistent with Case 1, this contrasting modal behaviour between bending and torsional motions matches the observations from the frequency domain analysis of Case 2 in Fig. 14.

The frequency- and time-domain analyses consistently demonstrate that, when the magnetic field is applied in multiple directions, the symmetric and non-proportional electromagnetic damping matrix leads to coupling between bending and torsional vibrations. Furthermore, the spectrogram representation in Figs. 17 and 20 provides further insight into this phenomenon. In particular, the spectrogram in Fig. 17 reveals how energy initially concentrated in bending-dominated frequency components progressively appears in frequency bands associated with torsional motion. This observation is consistent with the physical interpretation discussed in the frequency response analysis, where the electromagnetic forces induced by a multidirectional magnetic field do not act along a single mode but promote a redistribution of energy between coupled motions. Although the total energy of the system is continuously dissipated due to electromagnetic damping effects, the spectrograms show that this dissipation is accompanied by a transfer of energy across modal contributions, which explains the observed trade-off in the attenuation of bending and torsional responses. These findings highlight the importance of considering such coupling I in practical applications of eddy current damping, as overlooking it may lead to unsuspected behaviours or even counterproductive results.

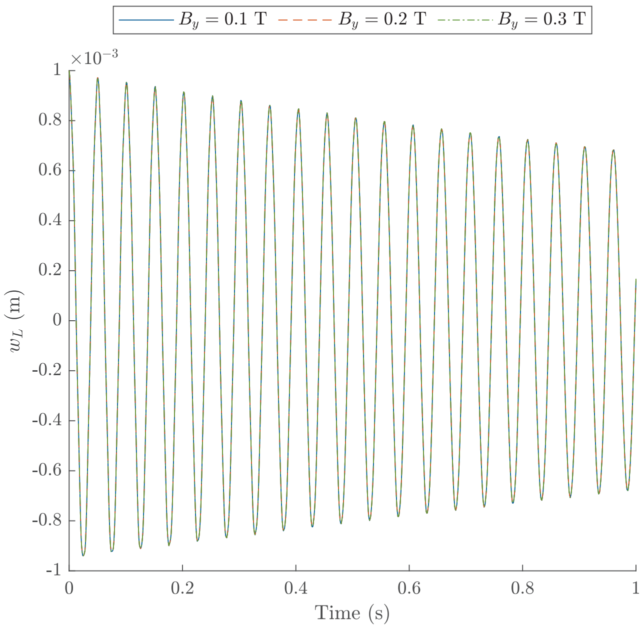

Fig. 18. Time response of the transverse displacement at the free end of the beam, $w_L(t)$, for Case 2. The solid, dashed, and dash-dot lines correspond to $B_y = 0.1$ T, $B_y = 0.2$ T, and $B_y = 0.3$ T, respectively. In all cases, B_x is fixed at 0.1 T.

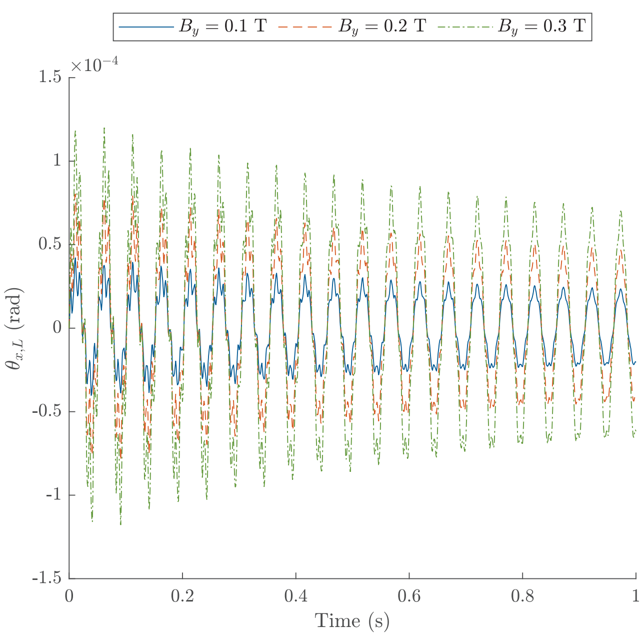

Fig. 19. Time response of the torsional rotation at the free end of the beam, $\theta_{x,L}(t)$, for Case 2. The solid, dashed, and dash-dot lines correspond to $B_y = 0.1$ T, $B_y = 0.2$ T, and $B_y = 0.3$ T, respectively. In all cases, B_x is fixed at 0.1 T.

7. Conclusions

This work has investigated the dynamic response of thin, non-magnetic, conducting beams subjected to static magnetic fields through a numerical framework that explicitly incorporates eddy-current-induced electromagnetic forces into the structural equations of motion, while neglecting self-inductance effects. The formulation incorporates velocity-dependent electromagnetic forces, derived from a finite-difference scheme, into a finite-element structural model for the beam's mechanical dynamics, ensuring consistent electromagnetic–mechanical interaction via Lorentz forces. This integration results in a symmetric, non-proportional electromagnetic damping matrix, which provides a systematic and physically consistent means to quantify and interpret eddy current effects in structural vibrations. The proposed formulation has been validated against experimental transmissibility data, showing excellent agreement between numerical and experimental results, and confirming its capability to accurately predict the electromagnetic–mechanical response of systems with eddy current damping.

Application of the proposed methodology to a specific beam in a cantilever configuration has demonstrated that the magnitude of the applied magnetic field components strongly influences the resulting vibrational behaviour. A key finding is that bending and torsional motions become dynamically coupled when the magnetic field is applied simultaneously in multiple directions, a phenomenon that does not arise under unidirectional field conditions. This interaction highlights the non-trivial nature of the electromagnetic–mechanical coupling and represents a natural extension of previously reported two-degree-of-freedom analyses to a multi-degree-of-freedom system. It reveals a complex interdependence between magnetic-field-induced damping, modal coupling, and overall vibration attenuation efficiency.

Frequency-domain results show that under multidirectional magnetic field excitation, increasing the magnitude of a given field component may lead to enhanced attenuation of bending motion at the expense of reduced damping in the torsional response, or vice versa, depending on which field component is increased. Furthermore, when the magnetic field enhances bending modal damping, peak attenuation is observed to be nearly uniform across the considered modes. In contrast, cases of reduced damping result in non-uniform peak amplification, most pronounced in the fundamental mode. This behaviour reflects the frequency-dependent distribution of eddy currents and emphasises the inherently non-proportional nature of the induced damping mechanism.

Time-domain analyses further confirm the complex bending-torsion interaction arising from the electromagnetic–mechanical coupling. The free-vibration response of the beam, following an initial displacement closely aligned with the first bending mode, shows that a multidirectional field can produce a marked exponential decay of bending amplitudes, with higher magnetic field magnitudes generally leading to faster energy dissipation. However, the results also demonstrate that this attenuation depends largely on the magnitude of the magnetic field components and that, under certain conditions, the bending response may remain largely unaffected by increases in field magnitude. In all cases, torsional vibrations are induced and decay exponentially. The transient responses highlight the contribution of higher-order modes to the early torsional oscillations before the system evolves toward a regime dominated by the fundamental bending mode. These observations validate the proposed framework as a reliable tool for capturing and interpreting transient electromagnetic–mechanical interactions in conductive beams.

Overall, the proposed numerical framework establishes a rigorous and versatile methodology for analysing and predicting the dynamic response of conducting beam-like structures subjected to externally applied magnetic fields. Its ability to capture the coupled electromagnetic–mechanical behaviour makes it particularly valuable for the analysis and design of contactless damping systems, where vibration control is achieved through field-induced eddy currents rather than direct mechanical contact. By integrating the electromagnetic damping effects within the mechanical framework, the methodology improves predictive accuracy and deepens the physical understanding of energy dissipation mechanisms in coupled systems. Beyond beam-like structures, the proposed approach contributes to the broader field of mechanical system dynamics by providing a consistent computational basis for exploring and optimising multiphysics vibration control strategies in complex conductive structures.

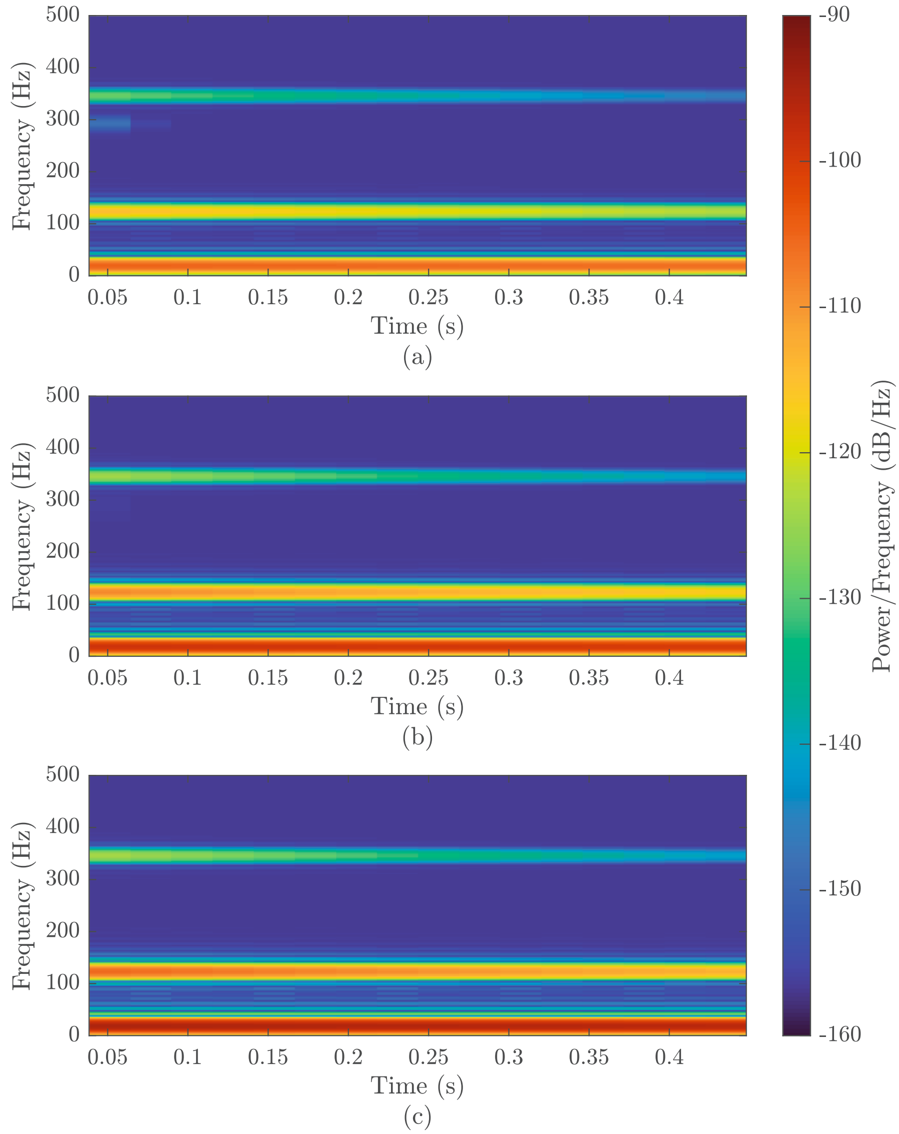

Fig. 20. Spectrograms of the torsional response for Case 2: (a) $B_y = 0.1$ T, (b) $B_y = 0.2$ T, and (c) $B_y = 0.3$ T.

8. Limitations and future work

Although the proposed numerical framework provides an efficient and accurate tool for analysing electromagnetic–mechanical coupling in thin conductive beams, several limitations should be acknowledged.

First, the eddy current density model relies on a thin-beam assumption, whereby the eddy currents are considered uniform across the beam thickness. As a result, skin depth effects are neglected, and the formulation may not be directly applicable to thick beams or to cases involving high-frequency excitations, where the penetration depth becomes comparable to the beam thickness. In addition, self-inductance effects are not included. While this simplification is justified for the frequency range and conductivity levels considered in the present study, it may limit the applicability of the model at higher frequencies, where secondary magnetic fields induced by eddy currents could become significant.

From a numerical perspective, the finite-difference scheme adopted for the electromagnetic problem assumes a uniform eddy current density within each cell. Although computationally efficient, this approximation may introduce local inaccuracies in the presence of strong field gradients. Furthermore, the mapping of electromagnetic forces and velocities between the two-dimensional finite-difference grid and the one-dimensional finite-element model assumes a consistent discretisation along the longitudinal direction. More general mapping strategies would be required to address non-conforming meshes or more complex geometrical configurations.

Future work will focus on extending the present formulation to account for thick beams and plate-like structures, as well as on incorporating self-inductance effects to enhance the model's range of applicability. Furthermore, a comprehensive parametric analysis would be required to generalise the findings of this work. In particular, investigating how key parameters, such as material conductivity and beam aspect ratio, influence both the damping rate and the intensity of the coupling phenomenon would provide valuable insights for the design and optimisation of engineering systems. In addition, further benchmarking against commercial multiphysics software, such as ANSYS or COMSOL, would provide a complementary validation of the proposed approach. On the experimental side, more complex boundary conditions and non-uniform magnetic field configurations could be investigated. The availability of a predictive numerical model also opens the door to optimisation studies in eddy current damping applications, including the design and positioning of magnetic devices. Finally, the coupling between nominally independent degrees of freedom under multidirectional magnetic fields, such as the bending-torsion interaction observed in this work, offers promising opportunities for further investigation in a wide range of engineering applications with eddy current damping.

Declaration of Generative AI and AI-assisted technologies in the writing process

During the preparation of this work the authors used ChatGPT in order to improve the language and readability of their paper. After using this tool, the authors reviewed and edited the content as needed and take full responsibility for the content of the publication.

CRediT authorship contribution statement

Mikel Brun: Writing – original draft, Software, Methodology, Formal analysis, Conceptualization. **Fernando Cortés:** Writing – review & editing, Methodology, Formal analysis, Conceptualization. **María Jesús Elejabarrieta:** Writing – review & editing, Methodology, Formal analysis, Conceptualization.

Declaration of competing interest

The authors declare that they have no known competing financial interests or personal relationships that could have appeared to influence the work reported in this paper.

Acknowledgements

This study has received financial support from the Department of Education of the Basque Government through the Research Group program IT1507-22 and from the Spanish Ministry of Science, Innovation and Universities through the project PID2024-158168OB-I00.

Appendix A

In this Appendix, the finite element mass and stiffness matrices employed in the formulation of the dynamic equations of motion are described. The beam is discretised into N_x elements, of length l_n, each of which is defined by two nodes. Given that the finite element formulation exhibits three degrees of freedom per node, each finite element possesses a total of six degrees of freedom. These correspond to the transverse displacement $v(t)$, the rotation about the x-axis $\theta_x(t)$, and the rotation about the z-axis $\theta_z(t)$, all of which are initially defined in a local coordinate system $x'y'z'$, as illustrated in Fig. A1a.

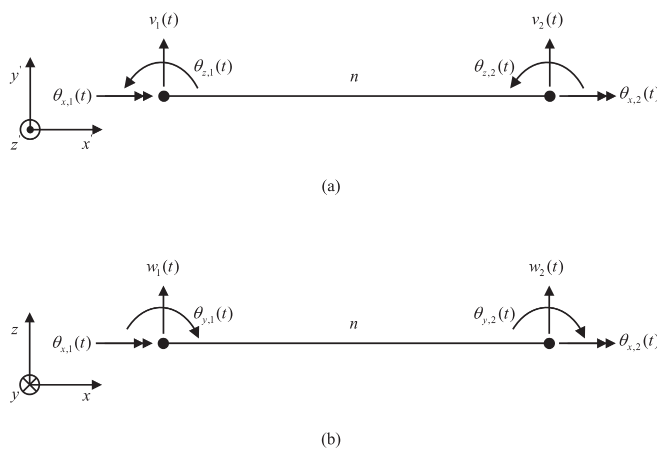

Fig. A1. Degrees of freedom of the n-th finite element: (a) local coordinate system; (b) global coordinate system.

Elemental mass and stiffness matrices in the local coordinate system.

In the local coordinate system, the generalised coordinate vector for the n-th finite element, $\boldsymbol{q}_{n,\mathrm{loc}}(t)$, is given by

$$\boldsymbol{q}_{n,\mathrm{loc}}(t) = [\, v_1(t) \quad \theta_{x,1}(t) \quad \theta_{z,1}(t) \quad v_2(t) \quad \theta_{x,2}(t) \quad \theta_{z,2}(t) \,]^{\mathrm{T}} \tag{A.1}$$

where the subscripts $(\bullet)_1$ and $(\bullet)_2$ denote the first and second node of the element, respectively.

The corresponding elemental mass matrix $\boldsymbol{M}_{n,\mathrm{loc}}$ is expressed as [42]

$$\boldsymbol{M}_{n,\mathrm{loc}} = \begin{bmatrix} 156m_{\mathrm{b}} & 0 & 22l_n m_{\mathrm{b}} & 54m_{\mathrm{b}} & 0 & -13l_n m_{\mathrm{b}} \\ 0 & 2m_{\mathrm{t}} & 0 & 0 & m_{\mathrm{t}} & 0 \\ 22l_n m_{\mathrm{b}} & 0 & 4l_n^2 m_{\mathrm{b}} & 13l_n m_{\mathrm{b}} & 0 & -3l_n^2 m_{\mathrm{b}} \\ 54m_{\mathrm{b}} & 0 & 13l_n m_{\mathrm{b}} & 156m_{\mathrm{b}} & 0 & -22l_n m_{\mathrm{b}} \\ 0 & m_{\mathrm{t}} & 0 & 0 & 2m_{\mathrm{t}} & 0 \\ -13l_n m_{\mathrm{b}} & 0 & -3l_n^2 m_{\mathrm{b}} & -22l_n m_{\mathrm{b}} & 0 & 4l_n^2 m_{\mathrm{b}} \end{bmatrix} \tag{A.2}$$

and the elemental stiffness matrix $\boldsymbol{K}_{n,\mathrm{loc}}$ is given by [42]

$$\boldsymbol{K}_{n,\text{loc}} = \begin{bmatrix} 12k_\text{b} & 0 & 6l_nk_\text{b} & -12k_\text{b} & 0 & 6l_nk_\text{b} \\ 0 & k_\text{t} & 0 & 0 & -k_\text{t} & 0 \\ 6l_nk_\text{b} & 0 & 4l_n^2k_\text{b} & -6l_nk_\text{b} & 0 & 2l_n^2k_\text{b} \\ -12k_\text{b} & 0 & -6l_nk_\text{b} & 12k_\text{b} & 0 & -6l_nk_\text{b} \\ 0 & -k_\text{t} & 0 & 0 & k_\text{t} & 0 \\ 6l_nk_\text{b} & 0 & 2l_n^2k_\text{b} & -6l_nk_\text{b} & 0 & 4l_n^2k_\text{b} \end{bmatrix} \tag{A.3}$$

The parameters in the above matrices are defined as

$$m_b = \frac{\rho_\text{v} b d l_n}{420} \tag{A.4}$$

$$m_t = \frac{\rho_v b d (b^2 + d^2) l_n}{72} \tag{A.5}$$

$$k_b = \frac{E(1 + \text{i}\eta) b d^3}{12 l_n^3} \tag{A.6}$$

and

$$k_t = \frac{G(1 + \text{i}\eta) c b^3 d^3}{(b^2 + d^2) l_n} \tag{A.7}$$

where the geometric factor c is obtained as a function of the ratio b/d as detailed in Table A1.

Table A1
Geometric factor c as a function of the ratio b/d [48].

b/d	1	2	4	8	∞
c	0.281	0.286	0.299	0.312	1/3

Transformation to the global coordinate system.

To formulate the system of equations in a global coordinate system xyz, as depicted in Fig. A1b, the local mass and stiffness matrices must be transformed accordingly. In the global coordinate system the degrees of freedom at each node are: the transverse displacement $w(t)$, the rotation about the x-axis $\theta_x(t)$, and the rotation about the y-axis $\theta_y(t)$. The generalised coordinate vector of the element in the global system for the n-th element, $\boldsymbol{q}_{n,\text{glob}}(t)$, is expressed as

$$\boldsymbol{q}_{n,\text{glob}}(t) = \begin{bmatrix} w_1(t) & \theta_{x,1}(t) & \theta_{y,1}(t) & w_2(t) & \theta_{x,2}(t) & \theta_{y,2}(t) \end{bmatrix}^\text{T} \tag{A.8}$$

and the relationship between the generalised coordinate vectors in the global and local coordinate systems are given by

$$\boldsymbol{q}_{n,\text{loc}}(t) = \boldsymbol{T}\boldsymbol{q}_{n,\text{glob}}(t) \tag{A.9}$$

where $\boldsymbol{T}$ represents the transformation matrix between the local and global coordinate systems. Consequently, the elemental mass and stiffness matrices in the global coordinate system, denoted as $\boldsymbol{M}_{n,\text{glob}}$ and $\boldsymbol{K}_{n,\text{glob}}$, respectively, are obtained via the transformations

$$\boldsymbol{M}_{n,\text{glob}} = \boldsymbol{T}^\text{T}\boldsymbol{M}_{n,\text{loc}}\boldsymbol{T} \tag{A.10}$$

and

$$\boldsymbol{K}_{n,\text{glob}} = \boldsymbol{T}^\text{T}\boldsymbol{K}_{n,\text{loc}}\boldsymbol{T} \tag{A.11}$$

where $\boldsymbol{T}$ is given by

$$\boldsymbol{T} = \begin{bmatrix} 1 & 0 & 0 & 0 & 0 & 0 \\ 0 & 1 & 0 & 0 & 0 & 0 \\ 0 & 0 & -1 & 0 & 0 & 0 \\ 0 & 0 & 0 & 1 & 0 & 0 \\ 0 & 0 & 0 & 0 & 1 & 0 \\ 0 & 0 & 0 & 0 & 0 & -1 \end{bmatrix} \tag{A.12}$$

Assembly of global mass and stiffness matrices

The global system matrices are constructed by assembling the transformed elemental contributions over all elements. The global mass and stiffness matrices, $\boldsymbol{M}$ and $\boldsymbol{K}$, are formulated as follows

$$\boldsymbol{M} = \sum_{n=1}^{N_x} \boldsymbol{M}_{n,\mathrm{glob}} \tag{A.13}$$

and

$$\boldsymbol{K} = \sum_{n=1}^{N_x} \boldsymbol{K}_{n,\mathrm{glob}} \tag{A.14}$$

It is noted that the global system comprises N_x +1 nodes, with the degrees of freedom appropriately assembled to ensure continuity and compatibility between adjacent elements.

Appendix B

This Appendix presents the procedure for computing the dynamic response of a second-order differential equation using the Newmark method. This method is a widely used implicit time integration scheme for solving second-order differential equations. It is conditionally stable and allows control over numerical damping, making it particularly suitable for solving dynamic problems that involve structural damping.

The general second-order differential equation governing the system's dynamics is given by

$$\boldsymbol{M}\ddot{\boldsymbol{q}}(t) + \boldsymbol{C}\dot{\boldsymbol{q}}(t) + \boldsymbol{K}\boldsymbol{q}(t) = \boldsymbol{F}_{\mathrm{ext}}(t) \tag{B.1}$$

where t denotes time, $\boldsymbol{M}$ is the mass matrix, $\boldsymbol{C}$ is the damping matrix, $\boldsymbol{K}$ is the stiffness matrix, $\boldsymbol{q}(t)$ is the nodal displacement vector, and $\boldsymbol{F}_{\mathrm{ext}}(t)$ is the external nodal force vector. The notation $(\bullet)^{\cdot}$ represents a time derivative.

To apply the Newmark method, initial conditions for $\boldsymbol{q}(0)$ and $\dot{\boldsymbol{q}}(0)$ must be specified, along with the external force vector $\boldsymbol{F}_{\mathrm{ext}}(t)$. The method approximates velocity and displacement using weighted averages of acceleration over discrete time steps Δt, expressed as [49]

$$\dot{\boldsymbol{q}}(t+\Delta t) = \dot{\boldsymbol{q}}(t) + [(1-\beta)\ddot{\boldsymbol{q}}(t) + \beta\ddot{\boldsymbol{q}}(t+\Delta t)]\Delta t \tag{B.2}$$

and

$$\boldsymbol{q}(t+\Delta t) = \boldsymbol{q}(t) + \dot{\boldsymbol{q}}(t)\Delta t + \left[\left(\frac{1}{2}-\alpha\right)\ddot{\boldsymbol{q}}(t) + \alpha\ddot{\boldsymbol{q}}(t+\Delta t)\right]\Delta t^2 \tag{B.3}$$

where α and β are parameters that influence the numerical stability and accuracy of the method. By solving Eqs. (B.2) and (B.3) at each time step, the Newmark method provides a step-by-step solution to the system's dynamic response. The full algorithm is outlined in Table B1.

Table B1
Step-by-step solution using Newmark integration method [49].

A. Initial calculations:

1. Form stiffness matrix $\boldsymbol{K}$, mass matrix $\boldsymbol{M}$, and damping matrix $\boldsymbol{C}$.
2. Initialise $\boldsymbol{q}(0)$ and $\dot{\boldsymbol{q}}(0)$, and compute $\ddot{\boldsymbol{q}}(0)$ from $\boldsymbol{M}\ddot{\boldsymbol{q}}(0) = \boldsymbol{F}_{\mathrm{ext}}(0) - \boldsymbol{C}\dot{\boldsymbol{q}}(0) - \boldsymbol{K}\boldsymbol{q}(0)$.
3. Select time step Δt and parameters α and β and calculate integration constants:

$$\beta \geq 0.50 \qquad \alpha \geq 0.25(0.5+\beta)^2$$

$$a_0 = \frac{1}{\alpha\Delta t^2} \qquad a_1 = \frac{\beta}{\alpha\Delta t} \qquad a_2 = \frac{1}{\alpha\Delta t} \qquad a_3 = \frac{1}{2\alpha} - 1$$

$$a_4 = \frac{\beta}{\alpha} - 1 \quad a_5 = \frac{\Delta t}{2}\left(\frac{\beta}{\alpha} - 2\right) \qquad a_6 = \Delta t(1-\beta) \qquad a_7 = \beta\Delta t$$

4. Form effective stiffness matrix $\widehat{\boldsymbol{K}} = \boldsymbol{K} + a_0\boldsymbol{M} + a_1\boldsymbol{C}$.

B. For each time step:

1. Calculate effective loads at time $t + \Delta t$:

$$\widehat{\boldsymbol{F}}_{\mathrm{ext}}(t+\Delta t) = \boldsymbol{F}_{\mathrm{ext}}(t+\Delta t) + \boldsymbol{M}(a_0\boldsymbol{q}(t) + a_2\dot{\boldsymbol{q}}(t) + a_3\ddot{\boldsymbol{q}}(t)) + \boldsymbol{C}(a_1\boldsymbol{q}(t) + a_4\dot{\boldsymbol{q}}(t) + a_5\ddot{\boldsymbol{q}}(t))$$

2. Solve for displacements at time $t + \Delta t$:

$$\widehat{\boldsymbol{K}}\boldsymbol{q}(t+\Delta t) = \widehat{\boldsymbol{F}}_{\mathrm{ext}}(t+\Delta t)$$

3. Calculate accelerations and velocities at time $t + \Delta t$:

$$\ddot{\boldsymbol{q}}(t+\Delta t) = a_0(\boldsymbol{q}(t+\Delta t) - \boldsymbol{q}(t)) - a_2\dot{\boldsymbol{q}}(t) - a_3\ddot{\boldsymbol{q}}(t)$$
$$\dot{\boldsymbol{q}}(t+\Delta t) = \dot{\boldsymbol{q}}(t) + a_6\ddot{\boldsymbol{q}}(t) + a_7\ddot{\boldsymbol{q}}(t+\Delta t)$$

Data availability

Data will be made available on request.

References

[1] S.S. Rao, Y.F. Fah, Mechanical vibrations, 5. ed. in SI units, Prentice Hall/Pearson, Singapore, 2011.
[2] B.M. Notaroš, Electromagnetics, International edition, Pearson, Upper Saddle River, NJ, 2011.

[3] Brun M, Cortés F, Elejabarrieta MJ. A methodology for analysing the influence of design variables in beams with eddy current damping. Mech Syst Sig Process 2025;234:112790. https://doi.org/10.1016/j.ymssp.2025.112790.
[4] Shobhana BB, Panchal VR, Matsagar VA. Research Developments of Eddy Current Dampers for Seismic Vibration Control of Structures. J Vib Eng Technol 2024;12:5953–71. https://doi.org/10.1007/s42417-023-01229-4.
[5] Diez-Jimenez E, Rizzo R, Gómez-García M-J, Corral-Abad E. Review of Passive Electromagnetic Devices for Vibration Damping and Isolation. Shock Vib 2019;2019:1250707. https://doi.org/10.1155/2019/1250707.
[6] Kriezis EE, Tsiboukis TD, Panas SM, Tegopoulos JA. Eddy currents: theory and applications. Proc IEEE 1992;80:1559–89. https://doi.org/10.1109/5.168666.
[7] Romero-Arismendi NO, Olivares-Galvan JC, Hernandez-Avila JL, Escarela-Perez R, Jimenez-Mondragon VM, Gonzalez-Montañez F. Past, present, and Future of New applications in utilization of Eddy Currents. Technologies 2024;12:50. https://doi.org/10.3390/technologies12040050.
[8] Turner LR, Hua TQ. Results for the cantilever beam moving in crossed magnetic fields, COMPEL - Int. J Comput Math Electr Electron Eng 1990;9:205–16. https://doi.org/10.1108/eb010076.
[9] Takagi T, Matsuda S, Tani J, Kawamura S. Analysis and experiment of dynamic deflection of a thin plate with a coupling effect. IEEE Trans Magn 1992;28:1259–62. https://doi.org/10.1109/20.123918.
[10] Brauer JR, Ruehl JJ. 3D coupled electromagnetic and structural finite element analysis of motional eddy current problems. IEEE Trans Magn 1994;30:3288–91. https://doi.org/10.1109/20.312640.
[11] Alonso Rodríguez A, Bertolazzi E, Ghiloni R, Valli A. Finite element simulation of eddy current problems using magnetic scalar potentials. J Comput Phys 2015;294:503–23. https://doi.org/10.1016/j.jcp.2015.03.060.
[12] Nagel JR. Fast finite-difference calculation of eddy currents in thin metal sheets. Appl Comput Electromagn Soc J 2018;33:575–84.
[13] Nagel JR. Finite-Difference simulation of Eddy Currents in Nonmagnetic Sheets via Electric Vector potential. IEEE Trans Magn 2019;55:1–8. https://doi.org/10.1109/TMAG.2019.2940204.
[14] Hiruma S. Extended Finite Element Method for Calculation of Eddy Currents at High Frequencies. IEEE Trans Magn 2023;59:1–4. https://doi.org/10.1109/TMAG.2023.3246629.
[15] Wang Y, Jiang X. Calculation of 3D transient Eddy current by the face-smoothed finite element–boundary element coupling method. High Volt 2020;5:747–52. https://doi.org/10.1049/hve.2019.0279.
[16] Hanser V, Schöbinger M, Hollaus K. A mixed multiscale FEM for the eddy current problem with T,Φ-Φ and vector hysteresis, COMPEL - Int. J Comput Math Electr Electron Eng 2022;41:852–66. https://doi.org/10.1108/COMPEL-02-2021-0053.
[17] Passarotto M, Pitassi S, Specogna R. Foundations of volume integral methods for eddy current problems. Comput Methods Appl Mech Eng 2022;392:114626. https://doi.org/10.1016/j.cma.2022.114626.
[18] Phan Q-A, Chadebec O, Meunier G, Guichon J-M, Bannwarth B. 3-D BEM Formulations for Eddy-Current Problems with Multiply-Connected Domains and Circuit Coupling. IEEE Trans Magn 2022;58:1–4. https://doi.org/10.1109/TMAG.2019.2954323.
[19] Kim W, Choi H. Immersed boundary methods for fluid-structure interaction: a review. Int J Heat Fluid Flow 2019;75:301–9. https://doi.org/10.1016/j.ijheatfluidflow.2019.01.010.
[20] Kabeel AE, El-Said EMS, Dafea SA. A review of magnetic field effects on flow and heat transfer in liquids: present status and future potential for studies and applications. Renew Sustain Energy Rev 2015;45:830–7. https://doi.org/10.1016/j.rser.2015.02.029.
[21] Dilgen CB, Dilgen SB, Aage N, Jensen JS. Topology optimization of acoustic mechanical interaction problems: a comparative review. Struct Multidiscip Optim 2019;60:779–801. https://doi.org/10.1007/s00158-019-02236-4.
[22] Shakeriaski F, Ghodrat M, Escobedo-Diaz J, Behnia M. Recent advances in generalized thermoelasticity theory and the modified models: a review. J Comput Des Eng 2021;8:15–35. https://doi.org/10.1093/jcde/qwaa082.
[23] Liu T, Cui Q, Xu D. Wind Turbine Composite Blades: a critical Review of Aeroelastic Modeling and Vibration Control. Fluid Dyn Mater Process 2025;21:1–36. https://doi.org/10.32604/fdmp.2024.058444.
[24] Liu J, Tan H, Zhou X, Ma W, Wang C, Tran N-M-A, et al. Piezoelectric thin films and their applications in MEMS: a review. J Appl Phys 2025;137:020702. https://doi.org/10.1063/5.0244749.
[25] Han Q, Xu X, Zhang Z, Yan Y, Peng C, Chu F. Dynamic characteristics of large permanent magnet direct-drive generators considering electromagnetic–structural coupling effects. Int J Mech Syst Dyn 2023;3:25–38. https://doi.org/10.1002/msd2.12065.
[26] Cortés F, Zarraga O, Cortazar-Noguerol J, Sarría I, Elejabarrieta MJ. Dynamic Behavior of a Two-Degree-of-Freedom System with Electromagnetic Interaction via a Skew-Symmetric Matrix. Int J Mech Syst Dyn 2025;5:579–95. https://doi.org/10.1002/msd2.70047.
[27] Zhu G-L, Hu C-S, Wu Y, Lü X-Y. Cavity optomechanical chaos. Fundam Res 2023;3:63–74. https://doi.org/10.1016/j.fmre.2022.07.012.
[28] Najar IA, Ahmadi R, Amuda AG, Mourad R, Bendary NE, Ismail I, et al. Advancing soil-structure interaction (SSI): a comprehensive review of current practices, challenges, and future directions. J Infrastruct Preserv Resil 2025;6:5. https://doi.org/10.1186/s43065-025-00118-2.
[29] Fang X, Li Y, Yue M, Feng X. Chemo-mechanical coupling effect on high temperature oxidation: a review. Sci China Technol Sci 2019;62:1297–321. https://doi.org/10.1007/s11431-019-9527-0.
[30] Niho T, Horie T, Uefuji J, Ishihara D. Stability analysis and evaluation of staggered coupled analysis methods for electromagnetic and structural coupled finite element analysis. Comput Struct 2017;178:129–42. https://doi.org/10.1016/j.compstruc.2016.09.003.
[31] Felippa CA, Park KC, Farhat C. Partitioned analysis of coupled mechanical systems. Comput Methods Appl Mech Eng 2001;190:3247–70. https://doi.org/10.1016/S0045-7825(00)00391-1.
[32] Keyes DE, McInnes LC, Woodward C, Gropp W, Myra E, Pernice M, et al. Multiphysics simulations: challenges and opportunities. Int J High Perform Comput Appl 2013;27:4–83. https://doi.org/10.1177/1094342012468181.
[33] Zhang J, Liu Y, Xue S. Analysis and experimental evaluation of an inertial eddy current damper for vibration control. Struct 2024;68:107052. https://doi.org/10.1016/j.istruc.2024.107052.
[34] Ferfecki P, Konečný M, Molčan M, Zapoměl J. Numerical simulation and Experimental Analysis of the magnetic Damping effect generated by a moving Magnet. Manuf Technol 2020;20:714–9. https://doi.org/10.21062/mft.2020.114.
[35] Sodano HA, Bae J-S, Inman DJ, Keith Belvin W. Concept and model of eddy current damper for vibration suppression of a beam. J Sound Vib 2005;288:1177–96. https://doi.org/10.1016/j.jsv.2005.01.016.
[36] Irazu L, Elejabarrieta MJ. A novel hybrid sandwich structure: Viscoelastic and eddy current damping. Mater Des 2018;140:460–72. https://doi.org/10.1016/j.matdes.2017.11.070.
[37] Shi Z, Shan J, Loong CN, Wu W, Chang C-C, Shi W. Experimental and Numerical Study on Dynamic Behavior of Eddy Current Damping with Frequency Dependence. J Eng Mech 2020;146:04020116. https://doi.org/10.1061/(ASCE)EM.1943-7889.0001852.
[38] Bae J-S, Kwak MK, Inman DJ. Vibration suppression of a cantilever beam using eddy current damper. J Sound Vib 2005;284:805–24. https://doi.org/10.1016/j.jsv.2004.07.031.
[39] Brun M, Cortés F, Elejabarrieta MJ. Numerical analysis of energy dissipation due to eddy currents in a vibrating beam. J Sound Vib 2025;595:118787. https://doi.org/10.1016/j.jsv.2024.118787.
[40] Brun M, Cortés F, Elejabarrieta MJ. Electromagnetic and structural dynamic coupling in a two-degree-of-freedom system. J Sound Vib 2025:119550. https://doi.org/10.1016/j.jsv.2025.119550.
[41] Li J, Chen B, Mao H. Exact closed-form solution for vibration characteristics of multi-span beams on an elastic foundation subjected to axial force. Struct 2024;60:105884. https://doi.org/10.1016/j.istruc.2024.105884.
[42] T.R. Chandrupatla, A.D. Belegundu, T. Ramesh, Introduction to finite elements in engineering, 4. ed., international ed, Pearson, Upper Saddle River, NJ, 2012.
[43] Notaroš BM. Total electromagnetic induction. In: Electromagnetics. Upper Saddle River, NJ: International edition, Pearson; 2011. p. 289–94.
[44] Siakavellas NJ. Analytical modelling of eddy currents induced by a time-varying magnetic field in a conductive plate, COMPEL - Int. J Comput Math Electr Electron Eng 1994;13:497–508. https://doi.org/10.1108/eb010131.
[45] Griffiths DJ. Introduction to electrodynamics. 4th ed. Boston: Pearson; 2013.
[46] Nagel JR. Numerical Solutions to Poisson Equations using the Finite-Difference Method. IEEE Antennas Propag Mag 2014;56:209–24. https://doi.org/10.1109/MAP.2014.6931698.
[47] Irazu L, Elejabarrieta MJ. Analysis and numerical modelling of eddy current damper for vibration problems. J Sound Vib 2018;426:75–89. https://doi.org/10.1016/j.jsv.2018.03.033.
[48] R.D. Blevins, Formulas for natural frequency and mode shape, Repr., reissue 1995, with minor corr, Krieger Publishing Company, Malabar, Florida, 1995.
[49] K.-J. Bathe, Finite element procedures, Prentice Hall, Englewood Cliffs (N. J.), 1996.